University of Alberta

Ablative Excitation of Surface Acoustic Waves in Aluminum Using UV Laser Pulses

by

James Paul Gospodyn   Ⓒ

A thesis submitted to the Faculty of Graduate Studies and Research in partial fulfillment
of the

requirements for the degree of *Master of Science*

Department of *Electrical and Computer Engineering*

Edmonton, Alberta
Fall 2002

Canada

University of Alberta

Library Release Form

Name of Author: *James Paul Gospodyn*
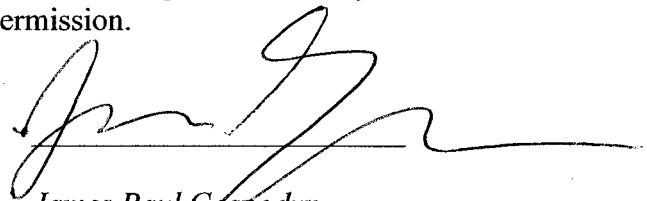
Title of Thesis: *Ablative Excitation of Surface Acoustic Waves Using UV Laser Pulses*

Degree: *Master of Science*

Year this Degree Granted: *2002*

James Paul Gospodyn
15304-100 Ave, Apt. 206
Edmonton, Alberta
T5P 0K6

Sept. 3, 2002

University of Alberta

Faculty of Graduate Studies and Research

The undersigned certify that they have read, and recommend to the Faculty of Graduate Studies and Research for acceptance, a thesis entitled *Ablative Excitation of Surface Acoustic Waves in Aluminum Using UV Laser Pulses* submitted by *James Paul Gospodyn* in partial fulfillment of the requirements for the degree of *Master of Science*.

R. Fedosejevs

Y. Y. Tsui

P. Schiavone

Sept. 3, 2002

"It's a dangerous business going out of your door. You step out into the road, and if you don't keep your feet, there is no knowing where you might be swept off to."

Bilbo Baggins, from
Fellowship of the Ring

Abstract

Surface acoustic wave generation using ablative excitation with ultraviolet laser pulses is studied experimentally in order to quantify the magnitude of response. The acoustic waves are interferometrically measured on the surface of polished aluminum samples at distances of 5 to 40 mm from the excitation spot. Amplitudes of the surface acoustic waves are measured as a function of laser energy (1-60 mJ) and distance from the excitation spot yielding peak-to-peak displacements of 1 to 40 nm. The results are compared to theoretical calculations using the Green's function for a step impulse response. The impulse required to match the measured results is compared to the expected impulse based on plasma pressure scaling in the ablative regime and the experimentally measured response is found to agree within a factor of about 1.7 with the theoretical predicted impulse.

Acknowledgement

I would first like to thank Dr. Robert Fedosejevs for giving me this wonderful opportunity. You have been an excellent teacher and supervisor and I am very grateful for all the doors that you have opened for me by taking me on as a student.

I would like to thank Dr. Arzu Sardarli for assisting in some of the experiments and for carrying out the model calculations.

I would like to thank Dr. Ying Tsui for his much appreciated assistance and discussions during the course of my project.

I would next like to thank all of the wonderful friends and colleagues I have made during this project, your countless discussions with me, both project and not-so-project related have been invaluable to me. Thank you Matt, "3 out of 3 Mikes" (Mike A., Mike T., Mike B.), Sean, Bin, Blair and Rick – whom I'd especially like to thank for the countless times I've needed your technical expertise, Roman, Serguei, Geoff, Chris, Cristina, Hong, Michelle, Dammika, Georg, Igor, Enyun.

Thank you to Alexei Brodnikovski for getting this project on its feet.

I would also like to thank the machine shop for their excellent metal works.

I would very much like to thank my Dad and brother for supporting me, and my Mom, whom I'm sure is supporting me where ever she may be.

Last but by no stretch of the imagination least, I would like to thank Catherine, for always being there – being there to smile when things are going great, and for cheering me up on the not-so-good days.

Table of Contents

List of Figures

Chapter 1 – Introduction

The study of laser-generated ultrasound in materials has been shown to be a powerful tool in the investigation of material parameters such as the elastic constants and grain sizes, which are related to the strength of the materials [1], [2]. Although the elastic properties of isotropic solids have been well studied for many years, the use of lasers to generate and detect acoustic waves in materials is important as a sensor application. This is due to the fact that, based on measurements of acoustic velocities, information relating to the elastic constants can be acquired relatively quickly online. However, in order to develop this technique as a sensor application, one must first quantify the form and amplitude of the acoustic wave for differing laser source conditions and geometries. The generation of large wave amplitudes is particularly important in the case of examining rougher materials with non-contact optical interferometry. In this case, techniques such as speckle interferometry, which requires deflections on the order of a tenth of the optical wavelength, may be required to detect the acoustic wave. Also, the quantification of real amplitudes would allow for measurements of scattering and attenuation of the acoustic wave, and thus may aid in quantifying inhomogeneities in the material. By generating very large acoustic waves, one can also measure nonlinear acoustic constants [3] as well.

The purpose of this study is to investigate the generation of large amplitude surface acoustic waves in bulk solids. There are many different acoustic wave modes which can be generated in materials, such as the longitudinal mode [4], shear mode [5], Rayleigh mode at an interface, and in thinner materials, Lamb modes [6], [7] to name a few. The advantage to using the Rayleigh or Surface Acoustic Wave (SAW) mode for the detection of material parameters is in single sided generation and detection, that is,

1

both the generation and detection of the SAW are done on one side of the surface of the material. This is advantageous in many respects since, for example in an industrial setting where materials would be moving along a conveyor belt, one does not need to remove or lift the sample to detect or generate an acoustic waveform. In fact, the SAW can be generated and detected while the sample is in motion at very high speeds [8].

Often, acoustic waves are generated in the thermoelastic regime [4], [9]-[12]. This occurs when the intensity of the laser is below the damage threshold for a given material. In this case, the generation of acoustic waves is purely non-destructive, since the acoustic waves are generated by a localized heating effect caused by the laser spot. Acoustic waves generated in this regime are much smaller (approximately 10 to 1000 times) than those as generated in the ablation regime by increasing the laser intensity past the breakdown threshold.

In the ablation regime for acoustic wave generation, a small amount of damage is done to the surface of the material, leaving a crater that is typically 10 to 100's of micrometers wide and 1 to 100 micrometers deep depending on the laser pulse energy. Often this amount of damage is tolerable in "non-destructive testing", since the damage spot is microscopic and often does not deleteriously affect the material. For example, in a scenario where one would be sorting scrap metals, a tiny amount of damage on the material surface is acceptable. Thus an important trade-off when using this acoustic generation technique is that a small amount of surface damage allows for the generation of SAWs with peak-to-peak amplitudes from 1 to 100's of nm. Since the most difficult aspect of the generation and detection of acoustic waves is in detection, the ability to generate large amplitude acoustic waves therefore is very important, particularly in

2

industrial situations where there is a larger amount of ambient thermal and mechanical noise, which leads to extraneous vibrations in the material.

It has been shown [13] that acoustic waves can be generated and/or detected using piezoelectric transducers rather than lasers. However, there are several advantages to using lasers for the generation and detection of acoustic waves. The first is that in the case of using piezoelectrics, a couplant material must be used which acts as a bonding media between the sample and the transducer and the acoustic wave is strongly dependent on the couplant material. This requires physical contact with the material and cannot be employed when measuring moving or high temperature materials. A second disadvantage of piezoelectric as an acoustic source/detector is in their size [1]. Often, it is desirable to perform acoustic measurements on smaller samples [14], and in confined geometries. The advantage to all optical generation and detection of acoustic waves is that one can overcome these limitations with relative ease. This relative ease is due simply to the fact that all-optical source and detection schemes are performed by imaging light to small probe spots in a non-contact geometry onto the sample surface. The calibration of an optical detector for measuring acoustic amplitudes is relatively easy, and all-optical means for generating acoustic waves yield more repeatable results.

The amplitudes of SAWs generated in the thermoelastic regime has been extensively studied and can be modeled based on the thermal and mechanical properties of the materials [15]. However, only a very limited number of results quantifying the amplitudes of the waves generated in the ablatively driven regime have been reported to date [16], [17]. These studies were carried out using infrared laser pulses, irradiating steel and aluminum surfaces. In this case, the generation mechanism that involves

3

plasma formation is more complex and much more difficult to model. It is expected for the excitation of the acoustic waves that the application of ultraviolet laser pulses will lead to better absorption and coupling to many materials, particularly for metals. Thus, the response to excitation with UV laser pulses is of particular interest.

The goal of this work is to investigate several aspects of the generation and propagation of UV laser induced SAWs in aluminum. It will be demonstrated using UV laser pulses that we are able to drive large amplitude waves, which have peak-to-peak amplitudes of up to 40 nm. The acoustic wave amplitude was measured as a function of laser pulse energy, from 1 mJ, where the source is weakly ablative, to 60 mJ where the source is strongly ablative. The variation of the acoustic pulse as a function of focal conditions was examined. The amplitude of the SAWs were also measured as a function of distance between excitation and probe spots. The results are compared to the calculated pulse amplitudes based on a linear response to a point-source excitation function. The impulse required to match the measurements is then compared to that expected due to plasma pressure impulse for the conditions of the experiment.

During the course of this study the supersonic blast wave in air generated by the laser plasma was also observed many microseconds after the SAW pulse. It is proposed that the surface normal pressure from the blast wave creates an inward surface displacement step on the order of a few nanometers, which remains as a tail to the SAW. In addition, the amplitude and arrival time of the observed signal from the supersonic blast wave can yield valuable information on the absorbed energy from the laser pulse and distance between excitation and probe spots.

Chapter 2 – Theory

2.1 – Laser Generation of Acoustic Waves in Materials

There are two regimes in which acoustic waves can be generated with a laser source. The first regime is the thermoelastic regime, in which the laser heats the material without melting or damaging the surface. The localized heating of the sample causes a localized stress in the material, which in turn produces various acoustic modes that propagate through the material. The second regime is the ablative regime. This regime occurs when the laser light causes the surface temperature to rise higher than the material's boiling point. Depending on the laser energy, the spot on the sample will be either vaporized or ionized producing a plasma spark. This study will examine the effects of the ablative regime as it relates to SAW generation.

By using a Q-switched laser pulse, the rate of energy deposition in the sample is too fast for significant thermal conduction to occur into the material during the laser pulse, thus the amount of material vaporized depends almost entirely on the latent heat of vaporization and the energy used in heating and ionizing the plasma. In this mode of ablation, several phenomena occur. First of all, the plasma exerts a high pressure on the surface, and vaporization and ionization of the material occurs in a high temperature front. Secondly, the plasma absorbs the light from the laser pulse heating up to very high temperatures and expanding away from the surface, reducing the direct energy flow into the target. And third, the expansion of the plasma acts as a normal force on the surface of the sample. In terms of laser generation of acoustic waves, the third phenomenon is the dominant effect [1]. It has been shown [18], that although the stress pulse applied to the

surface by the plasma has a rise time on the order of the laser pulse duration, the trailing edge is lengthened somewhat. The amplitude and frequency of the waves depend on the size and nature of the stress source. Typically in thick samples, there are several wave phenomena occurring, which is illustrated in Fig. 2.1.
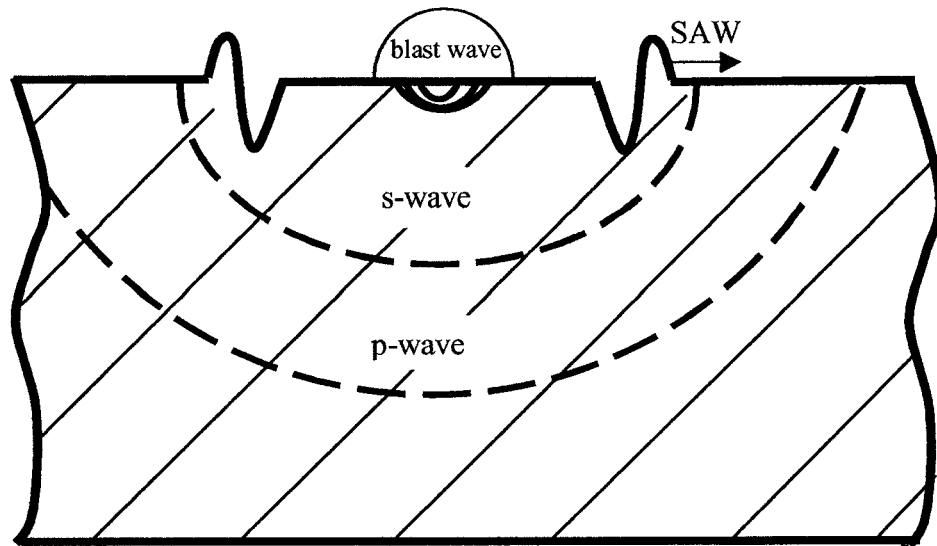
Fig. 2.1 – Illustration of the acoustic modes launched in the sample by the ablation process showing the p-wave, the s-wave, the surface acoustic wave (SAW) and the blast wave into the air.

The fastest acoustic mode, the p-wave or compressional wave is launched into the bulk of the material. This acoustic mode is followed by the s-wave, or shear wave. The shear wave is followed by the SAW, which only propagates along the surface of the sample.

In general, the displacement, u, of a particle at any point in an elastic solid, can be expressed in terms of a scalar potential Φ, and a vector potential Ψ as follows:

$$u = \nabla\Phi + \nabla\times\Psi \tag{2.1}$$

The two potentials satisfy the following equations:

6

$$\nabla^2 \Phi - \frac{1}{c_p^2} \frac{\partial^2 \Phi}{\partial t^2} = 0 \qquad (2.2)$$

$$\nabla^2 \Psi - \frac{1}{c_s^2} \frac{\partial^2 \Psi}{\partial t^2} = 0 \qquad (2.3)$$

where:

$$c_p = \sqrt{\frac{(\lambda + 2\mu)}{\rho}} \qquad (2.4)$$

$$c_s = \sqrt{\frac{\lambda}{\rho}} \qquad (2.5)$$

where c_p is the p-wave velocity, c_s is the s-wave velocity, λ is the Lamé elastic constant, μ is the shear elastic modulus, and ρ is the density of the material.

In the present case, one can consider the medium to be an infinite solid with only one boundary, commonly known as a half space. In this case, the boundary effects cause the generation of surface modes. One mode of interest is the Rayleigh or Surface Acoustic Wave, which expands radially along the surface. In a SAW, the motion of the surface particles is elliptical such that the normal motion of surface particles is typically 1.5 times the tangential displacement with respect to the surface plane. These displacements decay rapidly away from the surface into the bulk of the material. The normal displacement of a particle at a depth of one SAW wavelength, λ_R, is typically about 20% to 25% of the particle motion at the surface.

One may calculate the SAW propagation velocity c_R, from the equation [1]:

$$\left(2 - \frac{c_R^2}{c_s^2}\right)^2 - 4\left(1 - \frac{c_R^2}{c_p^2}\right)^{1/2}\left(1 - \frac{c_R^2}{c_s^2}\right)^{1/2} = 0 \qquad (2.6)$$

7

where only one solution gives a valid c_R. An approximate solution to the SAW propagation velocity is also given as [1]:

$$c_R = \frac{c_S}{1.14418 - 0.25771\nu + 0.12661\nu^2} \tag{2.7}$$

where ν is the Poisson's ratio in the material.

2.2 – Plasma Pressure Model

Since surface acoustic waves generated in the ablation regime can be described by a normal point force acting on the surface of a half space, in order to model the pressure and therefore impulse delivered to the target by the laser plasma, one must examine theoretical models for plasma pressure. An analytical model has been developed [19], which gives solutions to various plasma parameters such as the temperature and pressure in a plasma. The model was developed for two different geometries. The first regime would occur when a laser plasma is produced by a large laser spot, thus the plasma can be assumed to expand one dimensionally out of the plane of the target. The second regime would occur when a laser plasma is produced by a small laser spot, thus the plasma would expand spherically.

A simple analytical model based on a balance between energy absorption and work done in the expanding plasma was developed by Mora [19]. The absorption of low intensity radiation (with respect to a transition intensity which will be defined later) occurs primarily through an inverse bremsstrahlung process or collisional absorption.

The first assumption made is that the expanding electron density has an exponential profile in the absorption region, given by:

8

$$n_e = n_c \exp\left(\frac{-x}{L}\right) \tag{2.8}$$

where L is the density gradient length, and $n_c = \varepsilon_0 \, m_e \, \omega^2 \, e^{-2}$, where n_c is the critical density associated with the laser wavelength of frequency, ω. The second assumption is that the laser energy is absorbed by an inverse bremsstrahlung process. The third assumption is that the electron temperature, T_e (in units of eV), is estimated by equating the absorbed intensity, AI, to the energy necessary to maintain the exponential profile self-similar isothermal expansion from the critical density to the vacuum. That is:

$$AI = 4 n_c T_e c_i \tag{2.9}$$

where A is the absorption fraction, I is the incident laser intensity in units of Wcm^{-2}, c_i, the ion acoustic velocity is expressed as $c_i = (Z T_e / m_i)^{1/2}$, Z is the atomic number of the material and m_i is the mass of the ions.

One can then derive the inverse bremsstrahlung absorption for the density profile given by Eqn. 2.8, by using the WKB approximation as:

$$A = 1 - \exp\left(2 \int_C \mathrm{Im}(k) dx\right) \tag{2.10}$$

where the integral extends over the light path and back and where $k = \omega \varepsilon^{1/2}/c$, and ε is the complex dielectric constant, described by:

$$\varepsilon \cong 1 - \frac{n_e}{n_c} - i \left(\frac{n_e}{n_c}\right)^2 \frac{v_c}{\omega} \tag{2.11}$$

and v_c is the electron-ion collision frequency at the critical density, which is expressed as:

$$v_c = \frac{2}{3}\left(\frac{2}{\pi}\right)^{1/2} \frac{Z' n_c e^4 \ln \Lambda}{8 \pi m_e^{1/2} \varepsilon_o T_e^{3/2}} \tag{2.12}$$

9

where $\ln(\Lambda)$ is the Coulomb logarithm, Z is the average ion charge for a simple plasma, and is given by $Z' = \langle Z^2 \rangle / \langle Z \rangle$. By combining Eqn. 2.8, 2.10, and 2.11, one obtains the following expression for the absorption as:

$$A = 1 - \exp\left(-\frac{8}{3}\frac{v_c L}{c}\right)$$
(2.13)

Now, in order to develop solutions for parameters such as the ablation pressure, one would use Eqn. 2.9, 2.12, and 2.13, along with the expression for the scale length of the self-similar expansion of a 1-D isothermal plasma into vacuum, $L = c_i \tau$, where τ is the laser pulse duration, Mora [19] defines a transition intensity I^* above which inverse bremsstrahlung is not the sole absorption mechanism as:

$$I^* = 3.47 \times 10^8 \lambda_{\mu m}^{-5} \left(\frac{2Z}{A}\right)^{5/4} (\tau_{ns} Z' \ln \Lambda)^{3/2}$$
(2.14)

expressed in units of $W cm^{-2}$, where τ_{ns} is the laser pulse duration in nanoseconds, and $\lambda_{\mu m}$ is the laser wavelength in μm. Now, if one examines the case in which $I < I^*$ where the absorption is in the inverse bremsstrahlung absorption regime, one can derive expressions for various parameters such as the plasma temperature, maximum density reached by the laser radiation, and the parameter of interest in terms of acoustic wave generation, the ablation pressure. The ablation pressure for a 1-D planar expansion in units of Pa can be derived, from momentum balance and is double the thermal pressure in the plasma [19]. The ablation pressure is given by:

$$P_{Pa} = 205.14 \, I^{3/4} \lambda_{\mu m}^{-1/4} \left(\frac{2Z}{A}\right)^{-7/16} (Z' \ln \Lambda \tau_{ns})^{-1/8}$$
(2.15)

10

In the case of a small laser spot and long laser pulse, the expansion becomes spherically divergent and the 1-D planar expansion result is no longer valid. In this case the ablation pressure is described by Eqn. 2.16:

$$P_{Pa} = 27.9 \, I^{7/9} \lambda_{\mu m}^{-2/9} \left(\frac{2Z}{A} \right)^{-7/18} \left(Z' L_{\mu m} \ln \Lambda \right)^{-1/9} \tag{2.16}$$

where $L_{\mu m}$ is the radial exponential scale length parameter usually chosen as some fraction of the focal spot diameter in units of micrometers.

This ablation pressure is directed normal to the target surface and acts as the driving term to generate the acoustic waves in the medium.

2.3 – Modeling of Ablatively Driven SAWs

The model as it appears in the section was developed by other authors [20]-[22], and the calculations were carried out primarily by Dr. A. Sardarli. In order to model the SAW, the simplest solution form is for a step function force in time applied normal to the surface at a single point. Pekeris [20] considered this solution, which is consistent with the ablative regime in the plasma that creates a time dependent normal inward force at the surface of the half space.

The modeling of the ablative generation of a surface acoustic wave is a version of Lamb's problem, which is when a normal time-dependent point force (representing the plasma pressure) acts on the surface of a uniform half-space. Published references [1], [21] on this topic are based on calculations [20], [22] in which the time dependence of the normal and horizontal components of the displacement are calculated for a Heaviside step function force in time, which is pictorially represented in Fig. 2.2. This response can

then be used as the Green's function for calculating the response for a time-dependent

force function.

Heaviside Step Function
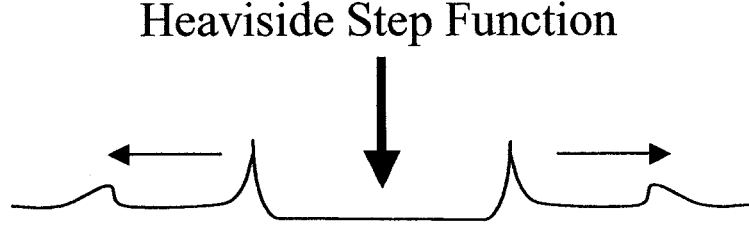
Fig. 2.2 – Pictorial representation of the surface acoustic wave generated by a Heaviside step function force impacting on the surface of a material. The force here acts much as a piston would impacting on the surface.

In the present calculations, the same Green's function was used, which was

described by equations (45)-(48) from Pekeris's work [20] for a material with a Poisson

ratio of $v = 0.25$ is employed. This Green's function is given by:

$$g(\tau) = \begin{cases} 0 & \tau < \dfrac{1}{k} & \text{(a)} \\[2ex] -\left[\dfrac{\pi}{96}\left(6 - \dfrac{k}{\sqrt{\tau^2 - 0.25}} - \dfrac{\sqrt{3k+5}}{\sqrt{0.75 + 0.25k - \tau^2}} + \dfrac{\sqrt{3k-5}}{\sqrt{\tau^2 + 0.25k - 0.75}}\right)\right] & \dfrac{1}{k} < \tau < 1 & \text{(b)} \\[2ex] -\left[\dfrac{\pi}{48}\left(6 - \dfrac{\sqrt{3k+5}}{\sqrt{\gamma^2 - \tau^2}}\right)\right] & 1 < \tau < \gamma & \text{(c)} \\[2ex] -\dfrac{\pi}{8} & \tau \geq \gamma & \text{(d)} \end{cases}$$

Eqn. 2.17

where c_p is the compression wave (p-wave) velocity, c_s is the shear wave (s-wave)

velocity, $k = c_p/c_s$, $\tau = c_s t/d$ (time normalized to the shear wave arrival time), d is the

distance from the epicenter to the observation location, and $\gamma = (3+3^{1/2})^{1/2}/2$ which

corresponds to the Poisson ratio $v = 0.25$, which comes from the assumption that the

material elastic constants λ and μ are equal. In this equation normalized time $\tau = 1$ corresponds to the arrival time of the shear wave and $\gamma\tau$ is the arrival time of the SAW.
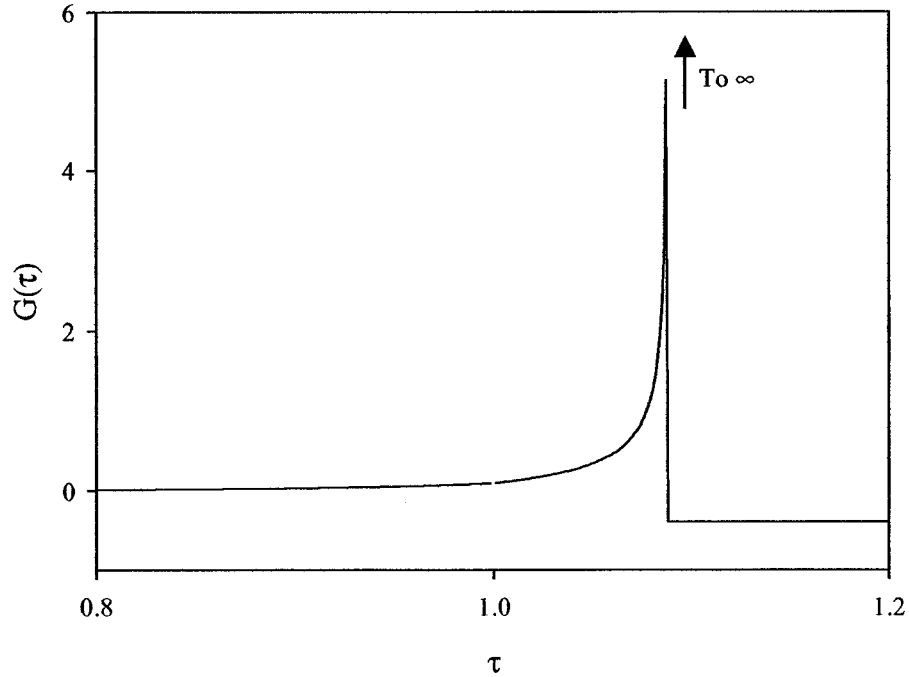
Fig. 2.3 – An example of the resultant Green's function for a point source step function in normalized time, τ.

Since for aluminum λ and μ are not equal ($\lambda = 58.1$ GPa, and $\mu = 26.1$ GPa) [1], the correct parameters are $\nu = 0.34$, $c_p = 6400$ ms^{-1}, $c_s = 3150$ ms^{-1}, $c_R = 2940$ ms^{-1}, $k = 2.03$, and from the acoustic velocities, one may calculate [1] $\gamma = 1.071$. As has been noted [21], changing the Poisson ratio doesn't affect the form of Eqn. 2.17 (c) and 2.17 (d), which correspond to the SAW part of the solution and in the form shown in Eqn. 2.17 are correct for any Poisson ratio. The (a) and (b) terms of Eqn. 2.17 correspond to the p- and s- wave parts of the wave specifically for a Poisson ratio of $\nu = 0.25$, and therefore should be modified to account for the new Poisson ratio of $\nu = 0.34$. However, the p- and s-

wave results were found to be small enough in the present results that they can be neglected.

To obtain the SAW waveform for a time dependent force $F(t)$, a technique was applied using the Duhamel integral [21] to calculate the time dependent normal displacement as:

$$u_0(\tau) = \int \frac{dF(\tau)}{d\tau}\bigg|_{\tau \,=\, \tau'} g(\tau - \tau')d\tau' \qquad (2.18)$$

where $F(\tau)$ is the normalized time dependence of the driving force. In the experimental case of a finite focal spot source, the force is effectively applied over a region of several hundred microns in size. The propagation time across the source spot (as determined by the SAW velocity divided into the laser spot size) is on the order of 100's of nanoseconds, which is much longer than the laser pulse duration of ~10 ns. Thus an effective pulsewidth for the excitation source pulse is used to account for the spatially extended excitation region. The comparison of calculated waveforms with experimental data has shown that the following simple $\cos^2$ function for the time dependent force allows for reasonable modeling of the data:

$$F(t) = \begin{cases} \cos^2\left(\dfrac{\pi t}{T}\right); & -\dfrac{T}{2} < t < \dfrac{T}{2} \\ 0; & t < -\dfrac{T}{2}, t > \dfrac{T}{2} \end{cases} \qquad (2.19)$$

where T is the base-to-base duration of the applied pulse in time.

The main parameter that characterizes the pulse – the total pulse width T can be estimated either by matching the experimental SAW parameters (for example the time duration between the peak positive excursion and peak negative excursion for the SAW)

or by calculating the SAW propagation time across the width of the focal spot in the direction of the SAW measurement, which will be discussed in Chapter 5.
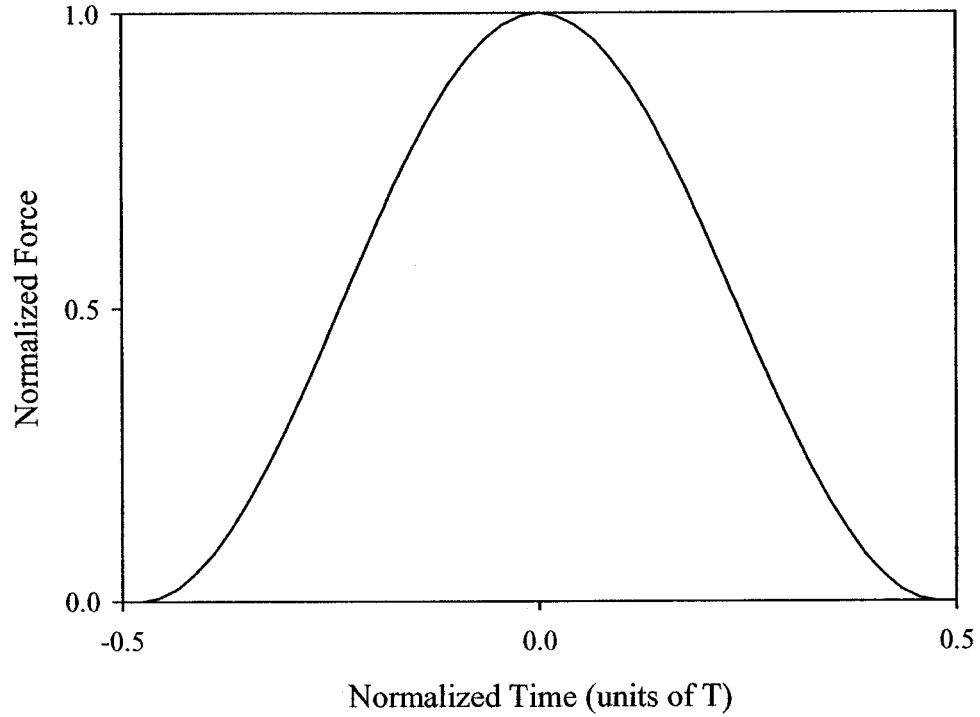
Fig. 2.4 – Plot of the $\cos^2$ applied force function used to model the laser pressure on the surface in normalized time and force coordinates.

To convert the result from normalized units to real time and force units, the following transformation is used:

$$u(t) = \frac{F_{Pk}}{\pi^2 \mu d} \left(\frac{c_p}{c_s} \right)^2 u_0(\tau) \qquad (2.20)$$

where F_{Pk} is the peak value of the real applied force, $u(t)$ and $u_0(\tau)$ are the displacements in real coordinates and normalized coordinates respectively, c_p and c_s are the p- and s-wave velocities respectively, and μ is the Lamé constant. Because of the singular nature of the Green's function, the values of displacement $u(t)$ are found numerically from Eqn. 2.20.

15

Chapter 3 – Experimental Details

3.1 – Aluminum Sample Preparation

Samples used for acoustic generation were made from 6061 alloy of aluminum (using laser induced breakdown spectroscopy to confirm the sample composition, see [23] for the technical details). There were a number of samples used throughout the course of the study, all of which were cut from the same block of aluminum. Each sample had an approximate area of 4.5×8 cm and an approximate thickness of 1 cm, which is sufficient for high frequency (i.e. >1 MHz) SAW generation, where the rule of thumb is that the sample thickness must be several times larger than the SAW wavelength since approximately 90% of the SAW energy is within a depth of one SAW wavelength into the sample. This avoids the production of Lamb wave (or plate wave) modes, which occur in thin samples. Since the SAWs generated in the present experiment are generally at higher frequencies than 1 MHz, the minimum sample thickness required should be $>>\lambda_R$ (1Mhz) $\cong$ 3 mm, if one were to assume a 1 MHz SAW frequency with an approximate velocity of 3×10^3 ms^{-1}.

The surface of the samples were first sanded with 100-grit sand paper and further sanded to a higher degree of smoothness with 600-grit sandpaper, which was lubricated with liquid dish soap and water. Finally, the samples were hand-polished with Brasso or in later experiments with Met-All Aluminum and Stainless Polish (polishing pastes), which gave the surfaces a shiny, reflective finish. Scanning electron microscope images were taken of a representative area of the sample in order to quantify the flatness of the samples after preparation.
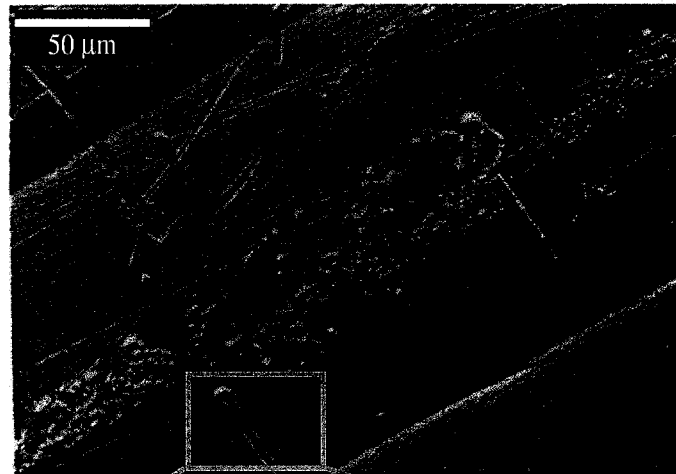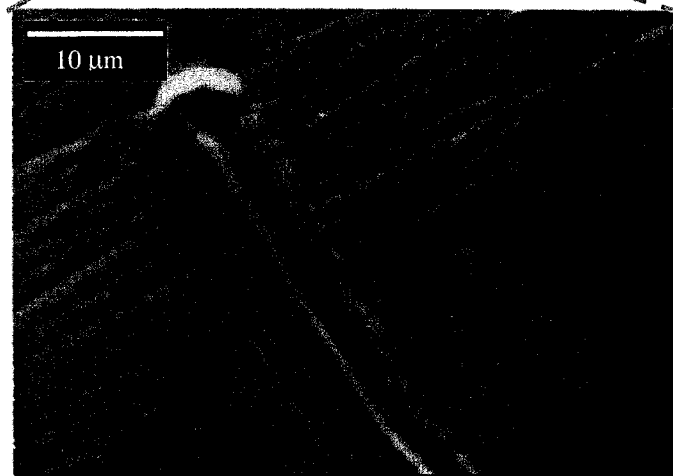
Fig. 3.1 – (a) SEM image of representative area of an aluminum sample, the white bar in the top left indicates a distance of 50 μm, and (b) SEM image of the highlighted area zoomed in. The white bar in the top left indicates a distance of 10 μm.

As can be seen in Fig. 3.1 (a) and 3.1 (b), which were typical images of the surface features, the sample is for the most part smooth to within 1 μm, however some larger features are scattered throughout which were due to grains from the sandpaper scratching the surface. This degree of smoothness was adequate to obtain a good

acoustic signal and probe beam reflection. The probe beam was focused to a small point

of approximately 20 microns on the surface of the sample with a microscope objective.

3.2 – Experimental Layout

The experimental layout for KrF laser SAW generation is shown in the following

figure:
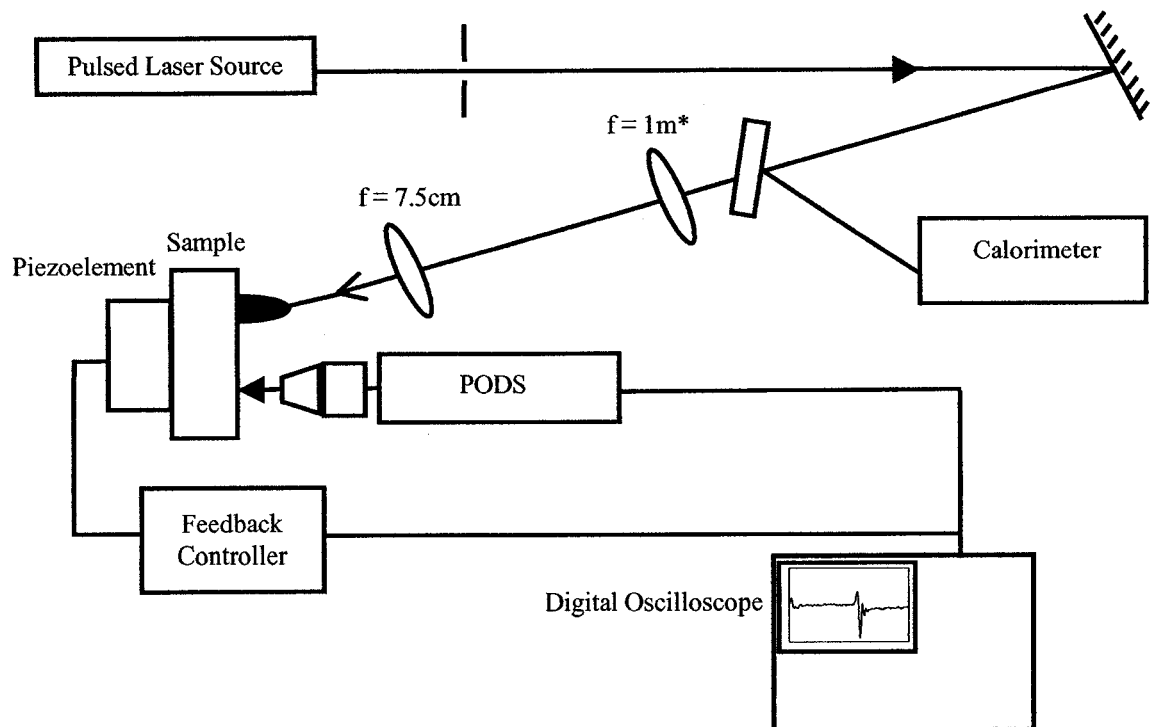
Fig. 3.2 – Experimental Layout, PODS (Precision Optical
Displacement Sensor) [24]. *Not present when the pulsed laser source
is the 4th harmonic Nd:YAG.

There were two pulsed laser sources used. The first was a KrF [25] excimer laser

operating at a wavelength of 248 nm with laser pulse energies in the range of 15 to 60 mJ

and pulse durations of 8 to 13 ns FWHM pulse duration. The pulse duration depended on

two factors: 1) the voltage across the laser head (i.e. laser energy), and 2) the amount of

use and age of the Kr, F, Ne gas mix in the laser head. Laser pulses produced by older gas led to shorter laser pulse durations as can be seen in Fig. 3.3.
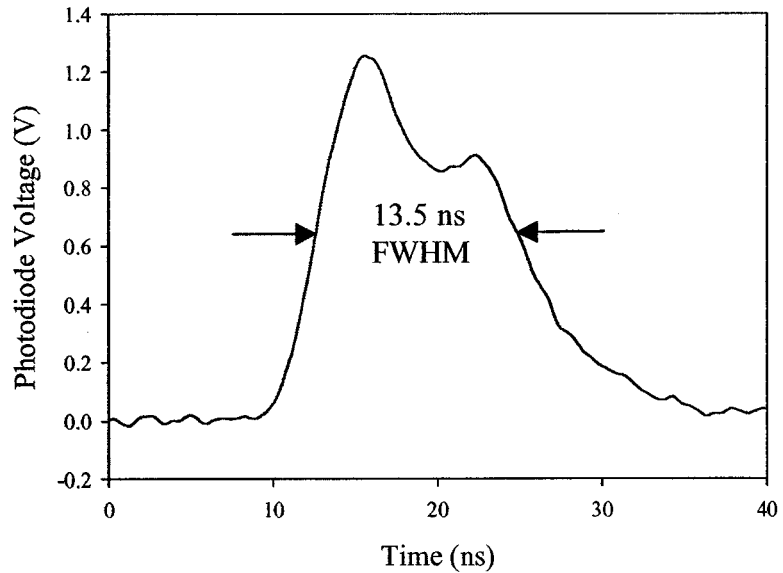
Fig. 3.3 (a) – Temporal profile of the KrF laser pulse firing at a discharge voltage of 35 kV with a fresh gas mix at a total pressure of 40 PSI. The laser pulse energy was approximately 65 mJ.
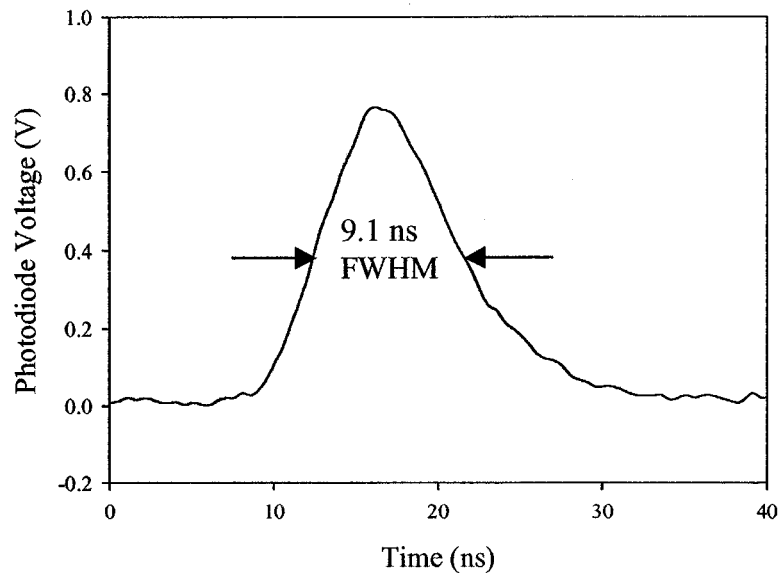
Fig. 3.3 (b) – Temporal profile of the KrF laser pulse firing at a discharge voltage of 35 kV with a gas mix at a total pressure of 40 PSI that is approximately 1 hr and 10 minutes old. The laser pulse energy was approximately 40 mJ.

As can be seen, with a fresh gas mix, as in Fig. 3.3 (a), there is a double peak, which causes the full width at half maximum (FWHM) for the pulse to be 13.5 ns, while in Fig. 3.3 (b), this peak disappears, and the FWHM for the laser pulse generated by the same breakdown voltage is 9.1 ns. Note also that, after 1 hour and 10 minutes of laser operation, there is approximately a 40% reduction in laser pulse energy from 65 mJ to 40 mJ. The second laser used was a 4th harmonic Nd:YAG laser [26] which operates at a wavelength of 266 nm with laser pulse energies in the range of 1 to 6 mJ, and pulse durations of 10 to 7 ns respectively.

The beam then propagates a distance of ~12 m and ~ 2 m for the cases of the KrF and 4th harmonic Nd:YAG lasers respectively to a quartz wedge, which reflects two beams of approximately 4% of the total laser energy to a calorimeter or photodiode for a measurement of energy delivered to the sample. In order to calibrate the calorimeter or photodiode in terms of energy delivered to the sample, the sample was replaced by another calorimeter with a known responsivity following the experiment and then a series of laser pulses were fired to obtain a good cross calibration of the laser pulse energy at the sample, and calorimeter/photodiode reading.

In the case of SAW generation by using the KrF laser, a pre-focusing quartz lens of focal length 100 cm was placed just after the wedge. Since the beam had apertured dimensions of ~9×26 mm at the input of the 100 cm lens according to burn marks on Dylux paper (a UV sensitive paper [27]), this first lens was used to gently converge the beam to a size of ~5×15 mm through a propagation distance of 45 cm, where a second quartz lens of focal length 7.5 cm and 2.5 cm diameter was placed. This second lens was

used to focus the beam into a small spot onto the sample at an incident angle of 30° from the sample normal.

In the case of SAW generation by the 4th harmonic Nd:YAG laser, the pre-focusing lens was not used, since the laser beam as it entered the 7.5 cm focal length lens had an elliptical size of approximately 3×4 mm according to burn marks on dylux paper.

The 7.5 cm focal length lens was placed on a translation stage, which allowed for translation of the lens along the path of the beam. In order to find the lens position at which best the focal point occurs at the surface of the sample, dylux burn paper was tightly fastened to the surface of the sample with the back side facing out. Since at and near focus, the laser spot is of high enough intensity that the spot would not appear on the paper, the less sensitive back side of the dylux was used, and the laser spots appeared as black spots on the white back side. Before the experiment was performed, the lens was traversed along its path while making single-shot burns onto the dylux paper. By measuring the laser burn spots on the dylux paper the best focal position could then be estimated to within 0.25 mm. As will be shown later, this degree of focusing was found to be adequate since the SAW amplitude varies only by a small amount with focal position within this focal region. The SAWs were then measured interferometrically using a precision optical displacement sensor (PODS) [24] after traveling across the surface to the detection point.

3.3 – PODS Theory of Operation

The PODS device [24], made by MPB Technologies, Inc. is a fiber-coupled interferometer used to measure real-time surface displacements on a sample. The

simplest interferometer for measuring displacement is a Michelson interferometer. In order to closer examine the theory of operation of the PODS device let us first examine the basics of a Michelson interferometer, and how the PODS uses this scheme to accurately detect small, ≥ 1 nm displacements.

In a Michelson interferometer [28], displacement is measured as a change in intensity at a detector. Schematically, the layout of a Michelson interferometer is as shown in Fig. 3.4:
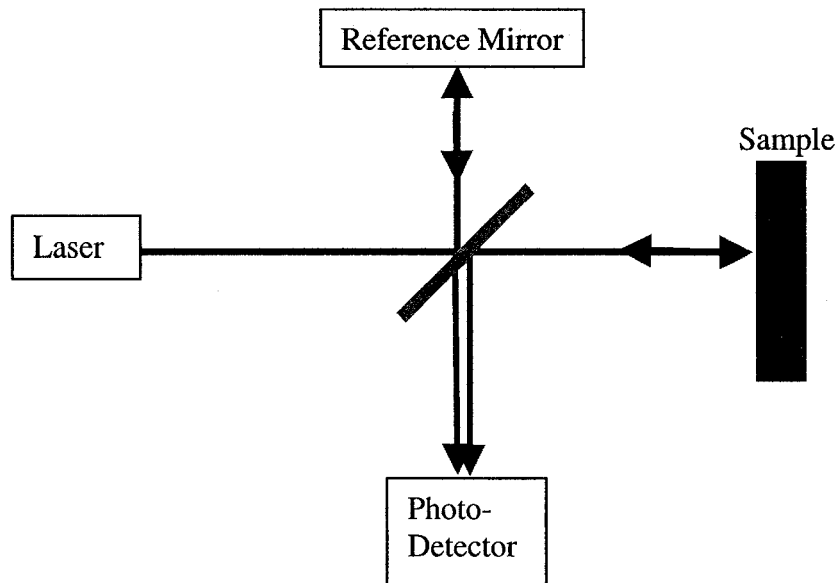
Fig. 3.4 – Schematic diagram of a Michelson interferometer.

As in Fig. 3.4, the laser output beam is split in two parts, optimally in half, at the beam splitter. One beam propagates towards the reference mirror and is sent back on itself, and the other beam is sent to the sample. The sample beam reflects off of the sample, and a portion is reflected on to the photo-detector (typically a photodiode, CCD camera, or power meter) with an intensity of I_1. The reference beam reflects off of the reference mirror, and a portion goes through the beam splitter to the detector with intensity of I_2.

Interference is determined by the difference in path lengths leading to an intensity at the photo-detector, assuming parallel planar wavefront beams, given by:

$$I = I_1 + I_2 + 2\sqrt{I_1 I_2} \cos(2kD) \qquad (3.1)$$

where $k = 2\pi/\lambda$, and D is the optical path length difference of the sample beam compared to the reference beam. If the reference beam path length is fixed then variations in the sample position lead to variations in the relative distance D and intensity I. It is also important to note that the intensity variation at the detector given by Eqn. 3.1 repeats every fringe, or when D increases or decreases by a multiple of $\lambda/2$.

The PODS device is somewhat more complicated, being a heterodyne interferometer. An example of a heterodyne Michelson interferometer is given in Fig. 3.5.
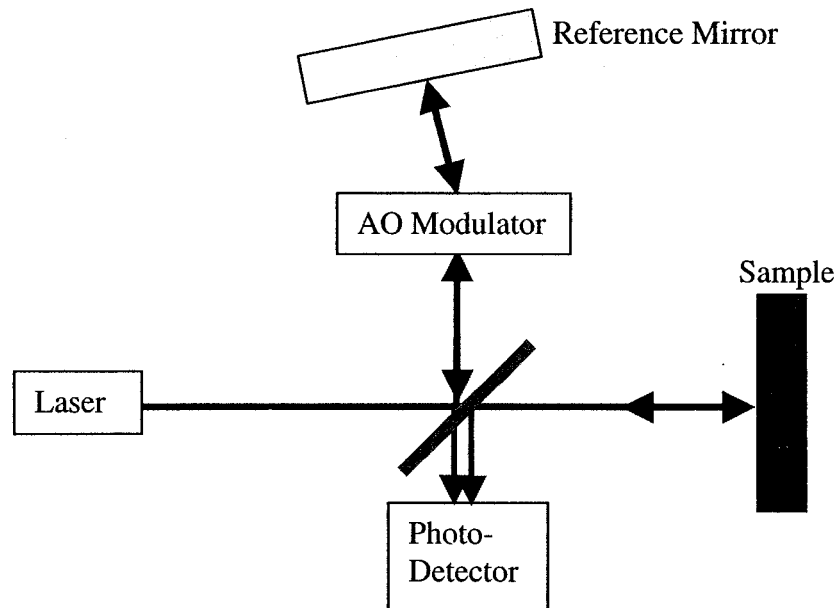
Fig. 3.5 – Schematic diagram of a heterodyne Michelson interferometer.

In this scheme, the beam in the reference arm is passed through an acousto-optic modulator that is driven at a specific frequency, which in the case of the PODS is 70 MHz. Thus, one can now think of the beam as having two frequencies, a beam in the

sample arm that is unperturbed at the original frequency ω_0 (the 0th order light), and the beam in the reference arm that is shifted by the driving frequency of the acousto-optic modulator $\omega' = \omega_0 + \Delta\omega$ (the 1st order output of the acousto-optic modulator). There are higher order outputs as well, which in this case are neglected since they are very small. Now, since there are two beams of light, one with a frequency of ω_0, and the other with a frequency of ω', using the superposition principle to determine the total electric field at the detector, one can calculate the intensity at the detector as:

$$I = I_1 + I_2 + 2\sqrt{I_1 I_2}\cos(2\Delta\omega t + 2kD) \qquad (3.2)$$

The factor of 2 in front of $\Delta\omega t$ is due to the fact that the beam in the reference arm travels through the acousto-optic modulator twice. It is important to note here that the optical path length displacement of the sample, D, is now determined by the phase shift of the $2\Delta\omega$ modulation signal. This scheme is beneficial since intensity fluctuations in the laser itself are no longer misread as a displacement as they would be in Eqn. 3.1, since the phase of the signal gives the displacement, not the intensity. The PODS sensor head layout consists of two Mach-Zehnder loops, one of which is the measure loop shown in Fig. 3.6, and the other is the reference loop. The actual system also contains a quarter wave plate in the beamline to the sample surface and a polarizing beam splitter cube. This is done to eliminate feedback into the laser source.
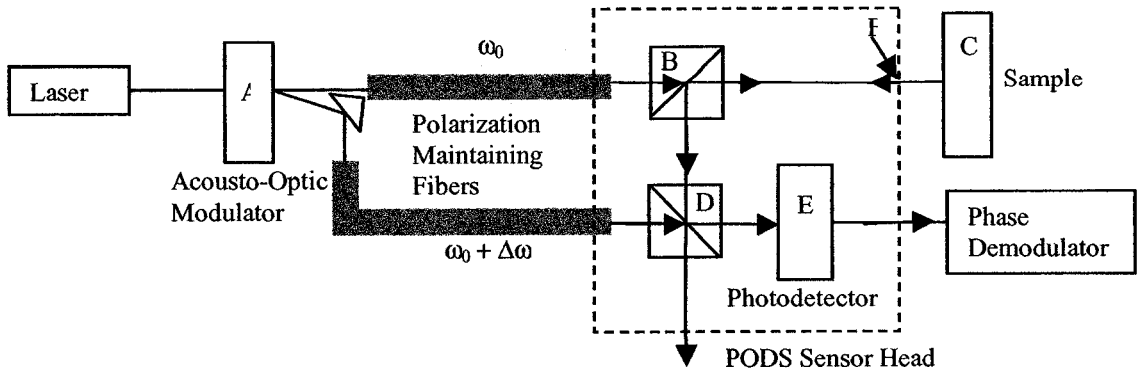
Fig. 3.6 – Simplified optical layout of PODS [30]

The path ABCBDE is the measure beam path for the measure loop, and the path ADE is the reference path for the measure loop. The reference loop would appear identical to the measure loop except for the fact that rather than outputting the beam to a sample, there is a mirror at the position indicated by F in Fig. 3.6 within the PODS Sensor Head. The light for this reference loop is split off from the two fiber signals entering the PODS sensor head. The output of this reference loop gives the phase reference signal compensated for environmental drifts in the fiber length and temperature. By applying Eqn. 3.2 without the factor of 2 in front of $\Delta\omega t$ since the light no longer makes two passes through the acousto-optic modulator, one would find the signals coming from the detector in the measure loop and reference loop to be:

$$V_m \cos(\Delta\omega t + \phi_m(t) + 2kD) \tag{3.3}$$

$$V_r \cos(\Delta\omega t + \phi_r(t)) \tag{3.4}$$

respectively, where $V_{m \text{ or } r} = 2K(I_1 I_2)^{1/2}$ for a detector with a conversion factor K [V/W], and $\phi_m(t)$ and $\phi_r(t)$ are the zero displacement phase shifts of the two signals. $\phi_m(t)$ and $\phi_r(t)$ are slowly varying in time as the temperature of the beam delivery fibers drift. However since they both propagate through the same fibers they drift together and $\phi_m(t) \cong \phi_r(t) + \phi_0$ where ϕ_0 is a constant. In Eqn. 3.3 and 3.4, the DC components were dropped

25

since they don't contain any displacement information. After some signal conditioning is applied to the measure and reference signal, they are combined into two different channels, one in which the measure signal is multiplied with the unshifted reference signal, and the other in which the measure signal is multiplied by a 90° shifted reference signal. One thus obtains two output channels, I (or in-phase channel) and Q (or quadrature channel) separated by 90°, given by:

$$I = V_0 \cos[2kD + \phi_0] \tag{3.5}$$

$$Q = V_0 \sin[2kD + \phi_0] \tag{3.6}$$

where V is approximately 0.9 volts for the Phase Demodulator used in the PODS. One can adjust the relative position of the sample through a feedback loop such that ϕ_0 is equal to $\pi/2$. In this case, when $D = 0$, $I = 0$ and $Q = V_0$. An advantage to having channels I and Q out of phase with each other by 90° is that one can track displacements that are larger than $\lambda/2$. However, in the present case the SAW displacements are much less than $\lambda/2$, thus it is only necessary to use the I channel output to measure surface displacements.

Ideally, for channel I and Q the peak voltages are $V_0 = 0.9$ V, and the two signals are exactly 90° out of phase. However, due to limitations and non-linearities in the demodulator circuit, these conditions are not perfectly met. Therefore, each PODS unit comes with its own set of calibration curves for channels I and Q. The I channel calibration data for voltage as a function of relative phase angle, is plotted in Fig. 3.7.
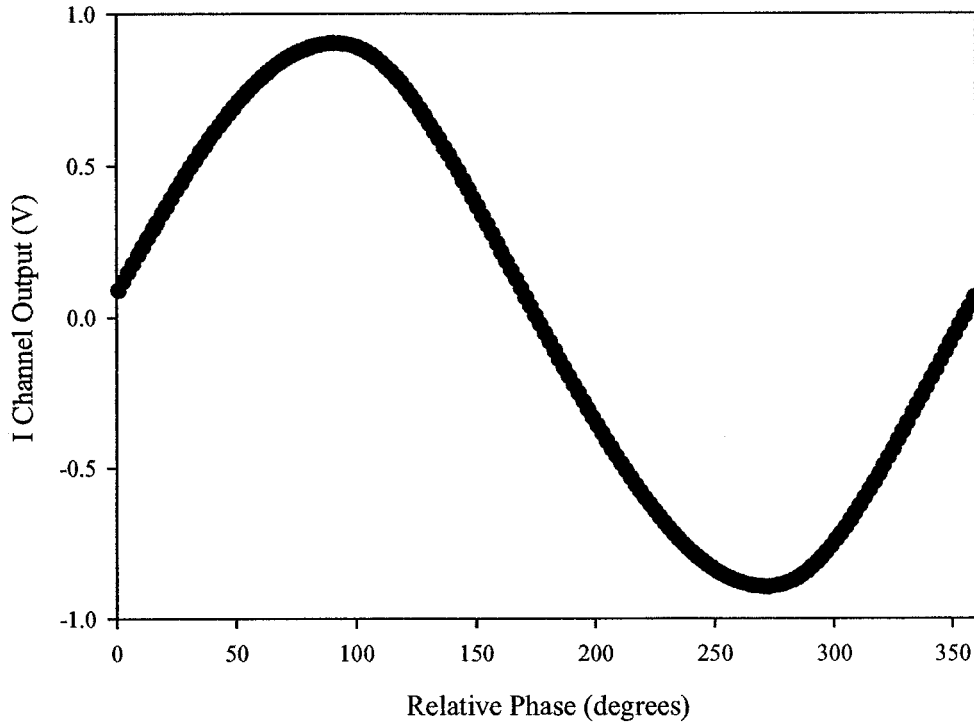
Fig. 3.7 – I channel calibration curve as a function of relative phase angle as specified by MPB Technologies [30].

By applying a regression on this data in order obtain the sinusoidal form of the calibration curve as shown in Fig. 3.7, we can solve for D in Eqn. 3.5 and obtain the conversion formula for surface displacement in nanometers, d_{nm}, as a function of the I channel voltage, I, as:

$$d_{nm} = 50.36\arcsin\left(\frac{I}{0.8872}\right)$$

(3.7)

Since the amplitudes of the SAW detected throughout the experiment were much less than $\lambda/2$, only the wideband channel I was used to measure the SAW displacements. The challenge to this approach however is that one must ensure that, through a feedback controller, that the sample position is locked into a relative position at or near the maximum response point on the signal curve. The bandwidth of the PODS detector is

27

specified as DC to 7 MHz in the wideband output mode as used here, and the noise

equivalent power of the PODS is specified as 0.4 pm/Hz$^{1/2}$ [30]. Thus for a 2 MHz SAW,

the minimum measurable displacement is 0.6 nm in a single shot acquisition.

3.4 – Feedback Control Circuit

The output voltage of the PODS Phase Demodulator for the I channel (or Q

channel for that matter), is controlled by the relative position of the sample, and

sinusoidally repeats every 316.4 nm, since the interferometric beam is obtained from a

HeNe laser of wavelength 632.8 nm. For the wideband output of channel I, the output

voltage ranges between approximately –0.9 and 0.9 V with the maximum response

occurring at an output voltage of 0 V. As shown in Fig. 3.7, if the starting position of the

sample gives an output voltage of 0 V, then a small deflection in sample position will

yield a larger deviation in phase demodulator output voltage. If the initial sample

position yields a demodulator output of ± 0.9 V, a small deflection in sample position

gives almost zero deviation in phase demodulator output.

Since the SAW amplitudes which are generated are on the order of 10 to 100

times smaller than the wavelength of the HeNe laser, it is necessary only to measure the I

channel output and to fix the initial sample position through the use of a feedback control

circuit such that the initial phase demodulator output voltage was fixed to a value at or

near 0 V. This was achieved by splitting part of the wideband I channel output to a

feedback control circuit, the output of which was connected to a piezoelectric PZT stack

onto which the sample was mounted. Since the feedback controller responds to

frequencies less than approximately 66 Hz, the stack was measured to have a

28

displacement that was linearly proportional to applied voltage given by $d_{nm} = 1.69 \times V$ at a

driving frequency of 20.2 Hz, $d_{nm} = 2.00 \times V$ at a driving frequency of 41.1 Hz, and

finally, $d_{nm} = 1.46 \times V$ at a driving frequency of 61 Hz, where d_{nm} is the expansion or

contraction in nanometers of the piezoelectric stack as a function of applied peak-to-peak

voltage, V. The average slope response was found to be $d_{nm} = 1.72$ nm/V. The results of

this measurement are shown in Fig.3.8.
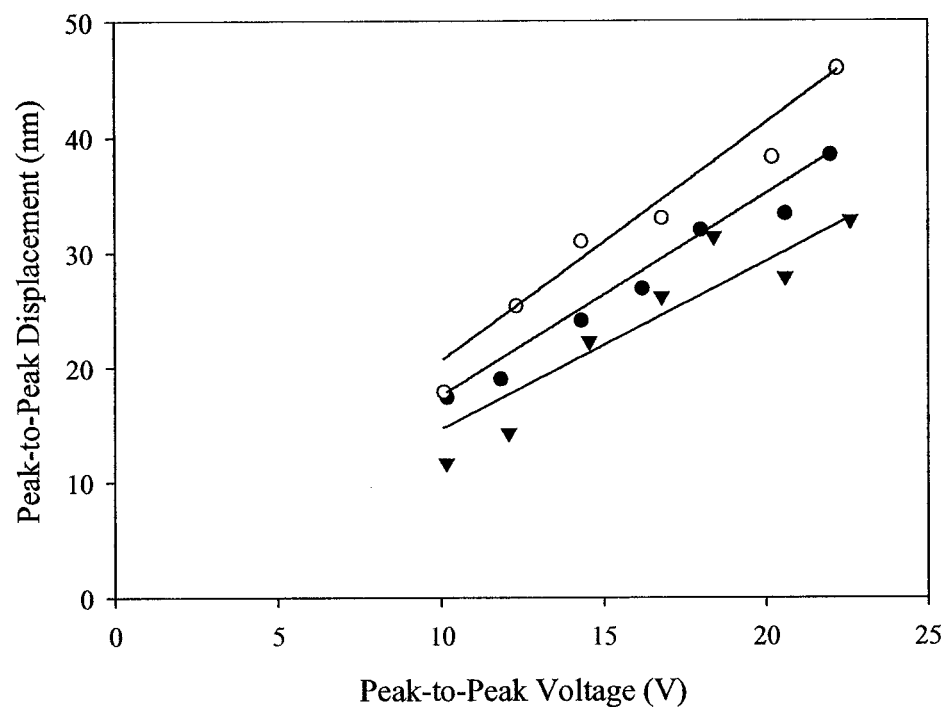
Fig. 3.8 – Peak-to-peak expansion or contraction of the piezoelectric element as a function of applied peak-to-peak sinusoidal voltage at a frequency of 20.2 Hz (solid circle), 41.1 Hz (hollow circle), and 61 Hz (solid triangle). The fits are least squares fits constrained to pass through the origin. The average slope is 1.72 nm/V.

In order to perform feedback control, the circuit was designed using the voltage

output of the I channel as the input signal which was integrated and amplified using a

voltage controlled high voltage module to give a control signal in the range of 0-300 V

DC on the piezoelectric element. A schematic diagram of the feedback control circuit is

shown in Fig. 3.9.
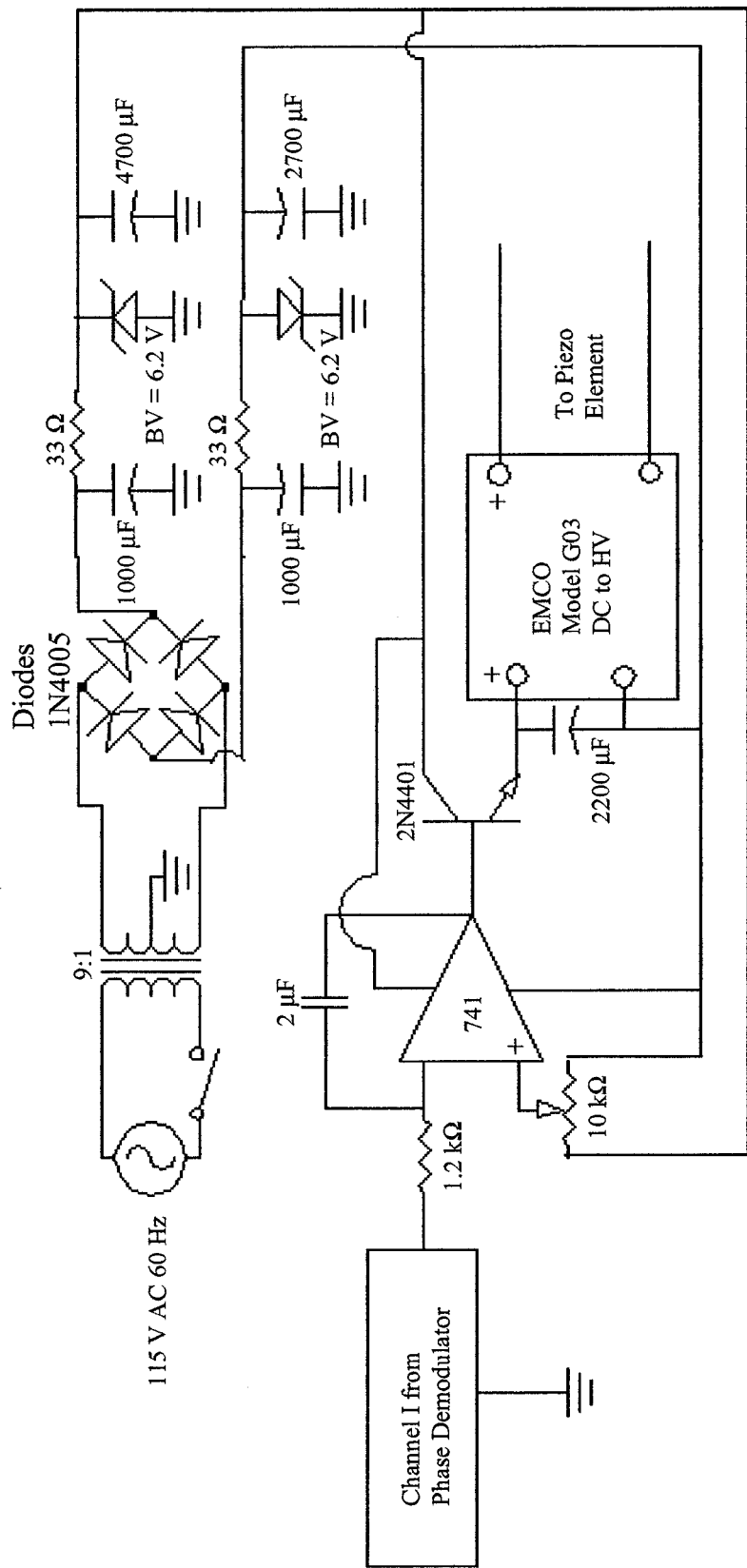
Fig. 3.9 – The Feedback Control Circuit with power supply

31

The signal from the PODS Phase Demodulator is connected to the inverting input of a 741 Op Amp, while the non-inverting input voltage is selectable through a potentiometer from −6 V to 6 V (from the power supply voltage). The adjustable voltage on the non-inverting input was necessary since the I channel signal can range from −0.9 to 0.9 V, while the required voltage input range for the EMCO Model G03 DC to HV DC amplifier was 0 to 12 volts. Since the EMCO DC to HV DC source will not amplify a negative input voltage, the adjustable voltage at the non-inverting input of the Op Amp offset the input voltage to the EMCO G03 module to a positive value. Another benefit for the adjustable offset on the non-inverting input was that the final voltage at which the I channel could be locked into (and therefore the relative sample position) is adjustable. In the above circuit configuration, the Op Amp acts as an integrator, where the expression which governs the output voltage of the Op Amp is [31]:

$$V_{out} = \frac{-1}{RC} \int \left(V_{in} - V_{pot} \right) dt \tag{3.8}$$

where V_{out} is the output voltage of the Op Amp, V_{pot} is the voltage at the non-inverting input of the Op Amp, V_{in} is the voltage at the inverting input of the Op Amp, $R = 1.2$ kΩ, and $C = 2$ μF. Note that in the present case that since the circuit is in a feedback loop, V_{out} is dependent on V_{in} and vice versa. From this, it can be shown that Eqn. 3.8 will converge to a specific value of V_{out} with V_{in} approaching V_{pot} over a long period of time. It is important to note that the RC time constant of the circuit built is 2.4 ms. Therefore, only variations which are much slower than this will be accurately tracked by the circuit. Once the circuit is turned on it will shift the sample position to a location corresponding to an input voltage approaching V_{pot} at which point the circuit converges. In practice if

the sample is moving rapidly or by a large amount, the circuit will not remain at a stable operating point.

The output of this integrator, which ranges from 0 to 12 V is connected through a 2N4401 BJT in a common collector configuration (see Fig. 5.19(a) in reference [31]). For a transistor, where I_B is the base current, and I_E is the emitter current, $I_E = (\beta+1)I_B$, where β is the short-circuit current amplification factor for the transistor. At the same time $V_E \cong V_B$, that is, the emitter voltage follows the base voltage. Thus, by using the common collector configuration the control voltage is passed on with an increase in the current going into an EMCO Model G03 DC HV source [32], which converts 0 to 12 V input into 0 to 300 V out with an input current of <250 mA at 12 V input (with a load).

3.5 – Data Acquisition and Analysis Technique

In order to acquire a good data set, first the best oscilloscope time scale setting appropriate for a given source-probe distance is determined by estimating the time of arrival of the SAW at the probe spot. The oscilloscopes used were the Tektronix 360 and 380 models with the 20 MHz bandwidth filter engaged. These models of oscilloscopes interface with a computer to output the voltage data with 8-bits of precision for each of the 1000 data points in the 20 time-division sweep period. The oscilloscope trigger point was set at 10% of the sweep period for the experiments so that approximately 90% of the acquired signal is data after the laser shot. The smallest possible time scale division setting was always used for a given source-probe distance. This was to obtain high precision in the data points corresponding to the SAWs detected. Using a LabView controller language that was used to interface with a Tektronix 300 series oscilloscope

33

through a GPIB card installed onto a PC, the oscilloscope was typically set to 100 mV per division for the voltage setting, since lower voltage settings give better precision for the analog-to-digital conversion and therefore more accurate determination of surface displacement.

In order to analyze the displacement data, a Microsoft Excel template file was employed. First, knowing the time scale per division that the oscilloscope was set at, one can determine the time division between data points to be 1/50 of the time scale per division. Next, in order to analyze the displacement data, Eqn. 3.7 was used to convert voltages to displacements. For all data points, the displacement of the first data point was subtracted away, thus setting a baseline displacement at 0 nm, for the beginning of the trace prior to the acoustic pulse.

Once the Microsoft Excel template evaluated the data, a new more realistic baseline was determined. The reason for this was that often, particularly in noisier experiments the relative sample position would drift during the course of the measurements, which could be caused by mechanical or thermal noise, or by electrical noise from the laser firing. Therefore, a number of data points, typically covering a period on the order of 100 nanoseconds was selected before the arrival of the SAW to give a new average baseline. Also, since these data points occur just before the SAW, the standard deviation of these data points from the average baseline could be used as the definition for the standard deviation measurement noise for the SAW peak positive and negative excursions.

3.6 – CCD Measurements of the Focal Spots

In order to compare the SAW response to laser intensity, let us first examine the intensity profile of both of the KrF and 4th harmonic Nd:YAG laser spots at and near best focus were determined. In order to measure the profile, a CCD camera (Electrim model EDC1000HR [33]) was used in place of the sample in the geometry shown in Fig. 3.10:
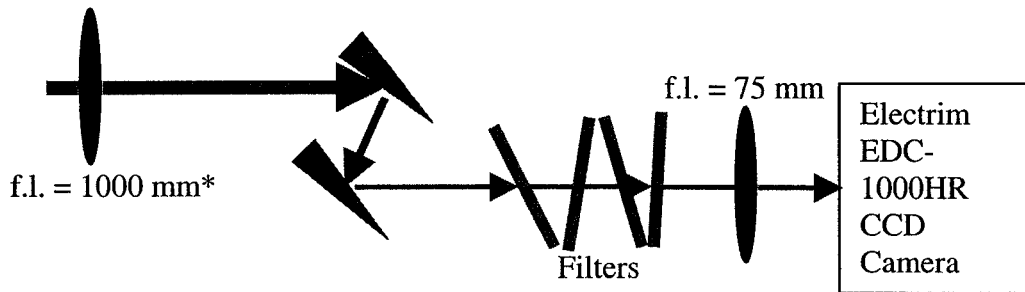
Figure 3.10 – Experimental Setup for the measurement of the focal spot profile. *Lens not present for the measurement of 4th harmonic Nd:YAG spot profile

In order to attenuate the beam energy to an amount that is non-damaging and detectable on the CCD, the beam was first reflected off of the front face of the two quartz wedges through Fresnel reflection in order to reduce the laser energy to a point that is below the damage threshold for metalized neutral density filters. Then up to 4 calibrated neutral density filters were employed, which were aligned at off-normal angles relative to the beam propagation axis in order to offset beam reflections within the filter system that would otherwise produce spurious images in the CCD camera. The entire system was carefully designed so that the total propagation distance that the beam travels is the same as in the SAW experiments. Two images were taken of the focused beam, one that did not saturate any pixels on the CCD camera, and another shot with one of the calibrated filters removed, which would overexpose the peak of the beam. The second shot would

more accurately resolve the low intensity outer profile of the beam. In knowing the calibrated optical density of the filters, the non-saturated image of the beam was multiplied by the optical attenuation factor of the removed filter, and then the values in the overexposed image that exhibited saturation were replaced by the corresponding values from the new pixel values from the non-saturated image. By doing so, the dynamic range of the camera was significantly enhanced.

3.6.1 – Measurement of the KrF laser spot

For the KrF laser, the CCD camera was used to measure a spot at best focus by using the aforementioned procedure. It is important to mention here that the horizontal pixel size used was 13.3 μm, and not the CCD Manual quoted pixel size of 11.5 μm. This is a correction for the fact that the CCD camera pixel array was normal to the incident beam, while in the SAW generation experiments, the angle of incidence of the beam on the sample was 30° from the sample normal in the horizontal plane.

In order to accurately determine the spot geometry and size, a contour plot of the intensity value as a function of position was generated for this image. The contour plot for the KrF laser spot at best focus is shown in Fig. 3.11. The size of the irradiation spot was determined using the 90% energy-containing contour. In this case, the intensity value that corresponded to the 90% energy-containing contour was 65.
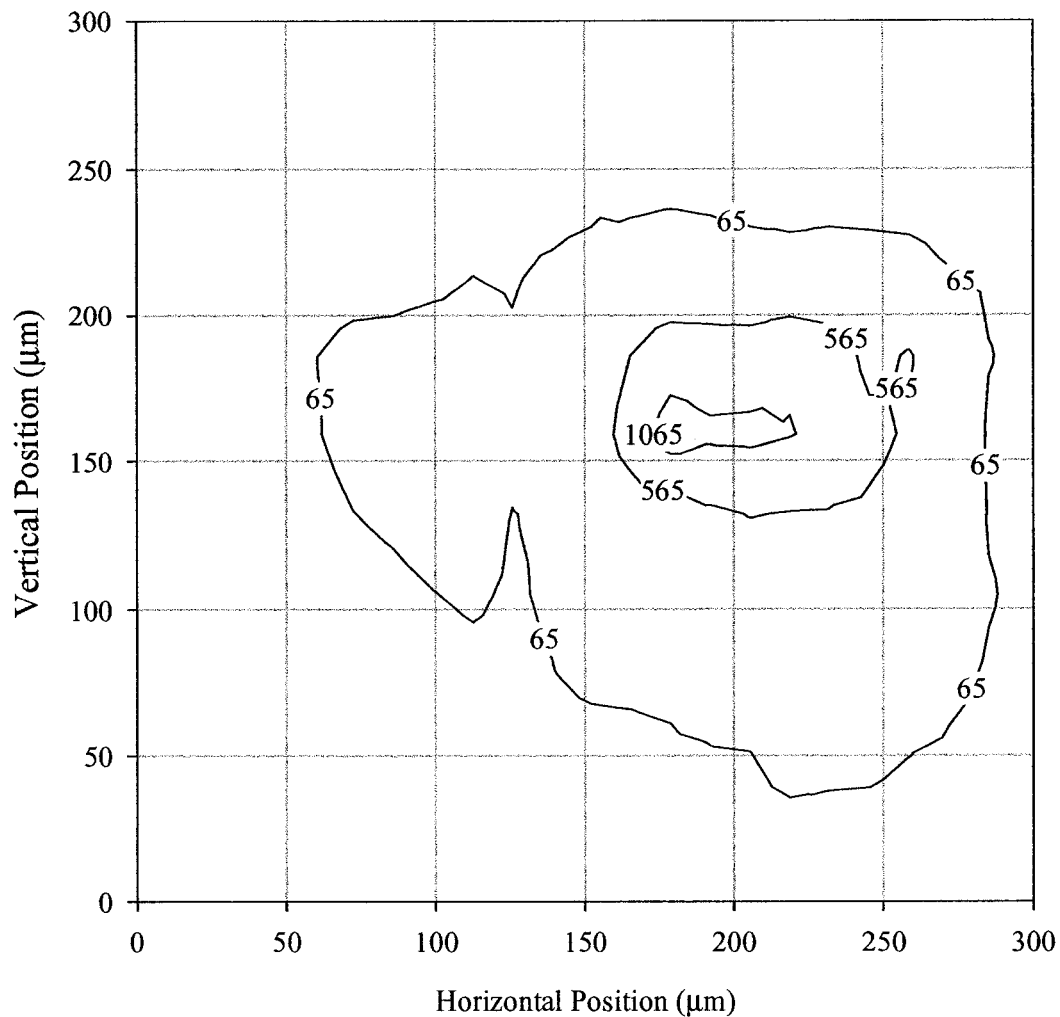
Fig. 3.11 – Contour plot illustrating the intensity distribution of the KrF laser spot at best focus as captured by the CCD camera. The intensity units are arbitrary. The intensity value of 65 is the boundary that contains 90% of the spot energy as determined by numerically integrating over the whole image.

By measuring the 90% energy-containing contour as shown in Fig. 3.11 and calculating the area contained within (based on the number of pixels within the 90% energy containing contour and pixel size of 13.3×27 μm), a 90% energy containing spot area is found to be 3.1×10^{-4} cm^2.

37

In comparison, the crater produced by the KrF laser pulses at best focus had a height and width of 330 μm and 395 μm respectively, and a spot area of 9.7×10^{-4} cm^2 at a laser energy of approximately 40 mJ and pulsewidth of 10 ns. A typical image of an ablation crater is shown in Fig. 3.12.
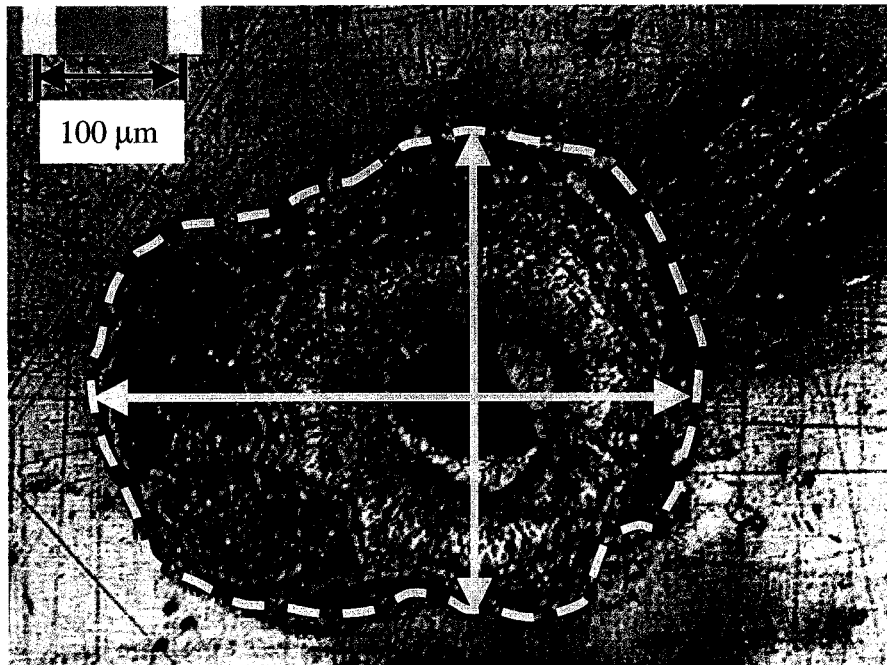
Fig. 3.12 – Optical microscope image of the ablation crater produced by a KrF laser with a 10 ns pulsed energy of approximately 40 mJ at best focus for the 75 mm focal length lens. The notches in the top right of the image shows a scale length of 100 μm.

It is important to note here that the crater which appears in Fig. 3.12 was produced by a beam which was rotated by 90° from the normal laser output beam, thus the height of the crater in this case would normally be the width, and vice versa. For the particular experiment that produced this crater, this was done since (as will be relevant later) the spatial profile in the vertical axis of the normal laser output is more symmetric. In this particular case, the crater area is 3.1 times larger than the laser spot area as determined by the CCD camera image. This is as expected, since the actual higher energy laser ablation

process would cause melting of the sample surrounding the ablation spot, thereby resulting in a crater that is larger than the actual spot size.

3.6.2 – Measurement of the 4th harmonic Nd:YAG laser spot

Now consider the 4th harmonic Nd:YAG produced spot. In a similar manner, the spot has a measured intensity contour as shown in Fig. 3.13, where an intensity value of 51 corresponds to the boundary for the 90% energy containing contour.
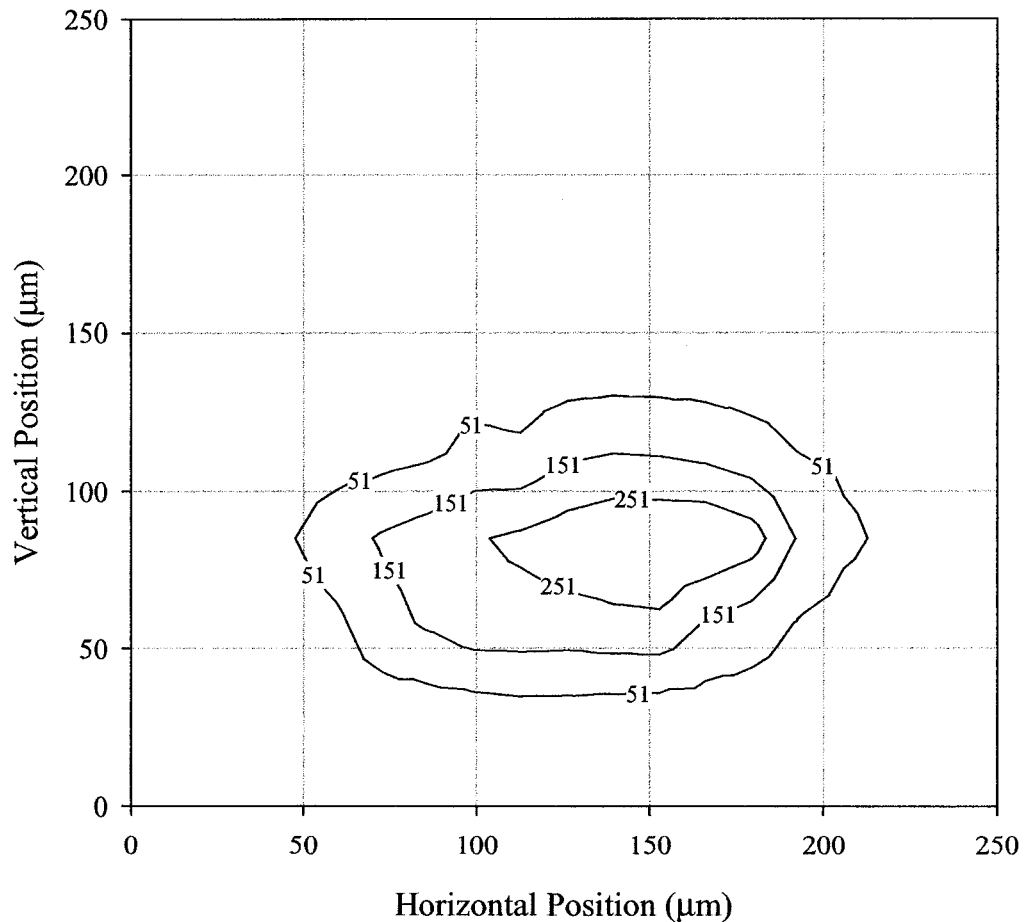
Fig. 3.13 - Contour plot illustrating the intensity distribution of the 4th harmonic Nd:YAG laser spot at best focus as captured by the CCD camera. The intensity value of 51 contour is the boundary that contains 90% of the spot energy.

The area within the 90% energy containing contour as shown in Fig. 3.13 is 8.3×10^{-5} cm^2.

For comparison the crater produced by the 4th harmonic Nd:YAG laser pulses, is shown in Fig. 3.14. At best focus, the ablation crater produced had a width and height of 180 μm and 130 μm respectively, and an area of 1.8×10^{-4} cm^2. The size and enclosed area are shown in Fig. 3.14. The ablation crater was produced by a 4.7 mJ laser pulse of approximately 7 ns duration for the 4th harmonic Nd:YAG laser.
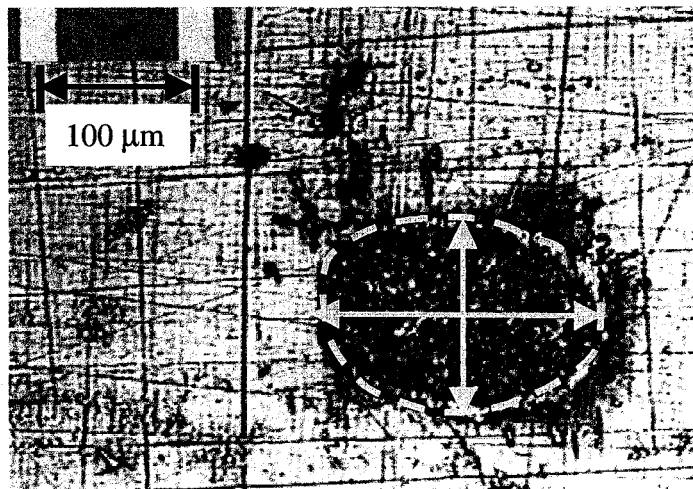
Fig. 3.14 – Optical microscope image of the crater produced by the 4th harmonic Nd:YAG at best focus for the 75 mm focal length lens. The scale in the top right indicates a distance of 100 μm.

The crater area in this case is approximately 2.2 times larger than the laser spot which was measured by the CCD camera, which again is as expected due to the melting of the sample in the region surrounding the laser spot.

The average intensities for a 40 mJ, 10 ns KrF laser pulse and a 5 mJ, 7 ns 4th harmonic Nd:YAG laser pulse are thus 1.2×10^{10} Wcm^{-2} and 7.7×10^{9} Wcm^{-2} based on 90% of the energy contained within the 90% energy contour. These intensities are significantly above the threshold for breakdown in aluminum which is in the range of 7×10^{8} Wcm^{-2} [34] for a 5 ns laser pulse with a wavelength of 266 nm.

40

Chapter 4 – Experimental Results[*]

4.1 – Characteristics of SAW

A typical ablatively driven SAW waveform is shown in Fig. 4.1. The waveform shown in Fig. 4.1 is an average of nine shots with a laser pulse energy of E_L = 4.7 mJ, as produced by the 4th harmonic Nd:YAG laser pulse with a distance from excitation spot to probe spot of d_{probe} = 5.1 mm. This experiment was performed by taking single shot data, that is, every laser shot was on an undamaged part of the sample. After obtaining multiple data sets all taken for the same source-to-probe distance, nine of the data sets were used in order to average out the noise in the signal. This was done carefully by matching up the point of zero crossing of the wave for each of the nine datasets. It was noticed that from dataset to dataset there was a minute variation up to approximately 20 ns for the time at which the point of zero crossing occurred. This fluctuation was caused by variations in the source-to-probe distance from dataset to dataset, which was attributed to the small adjustments in the position of the microscope objective that was used to focus the PODS probe beam onto the sample, and therefore to optimize the signal. This shot-to-shot variation in the source-to-probe distance was confirmed by making a precise measurement on the source-to-probe distance after every laser shot. The measured standard deviation for the fixed source-to-probe distance was found to be 48 μm for the nine datasets used for the average. Using the micrometer translation stage that the

---

[*] This chapter has largely been extracted from J. P. Gospodyn, A. Sardarli, A. M. Brodnikovski, and R. Fedosejevs, "Ablative generation of surface acoustic waves in aluminum using ultraviolet laser pulses", *J. Appl. Phys.* vol. **92**, pp. 564-571, 2002.

sample was mounted onto, the measurement of source-to-probe distance was made by

positioning the ablation crater under the PODS probe spot.
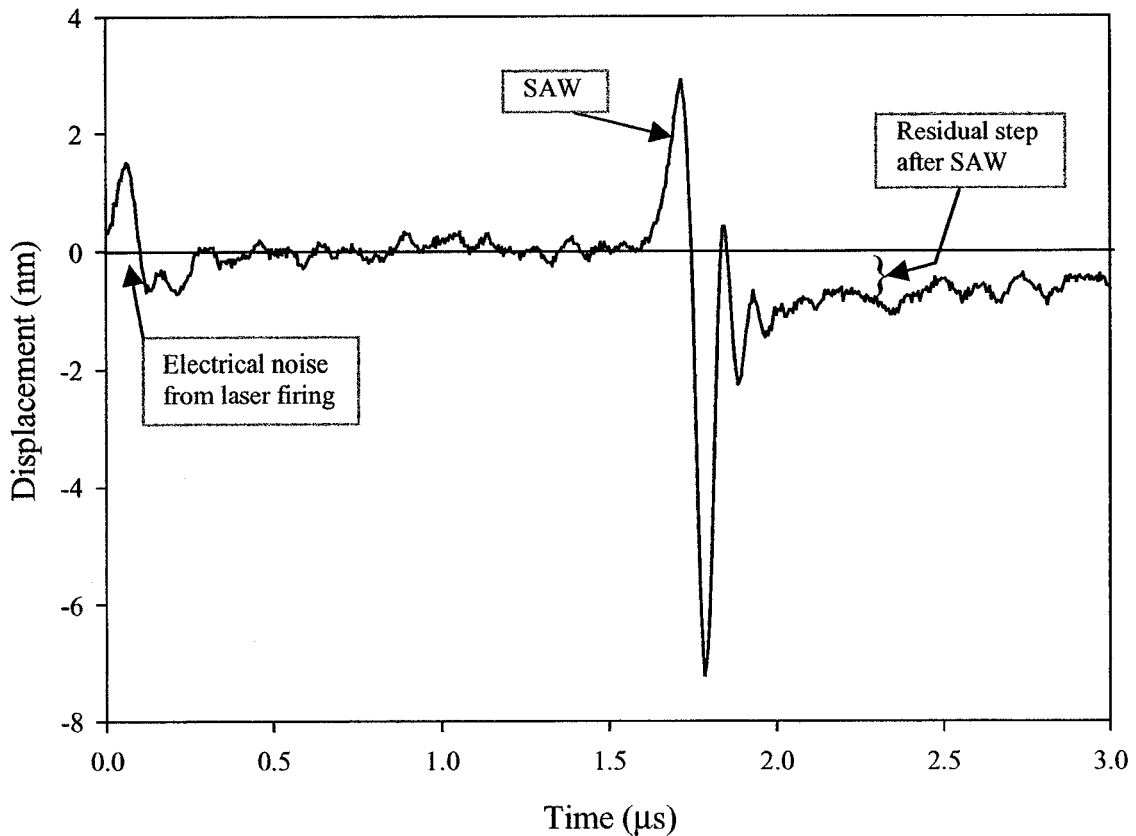
Fig. 4.1 – A typical SAW waveform. This result is an average of nine
shots of a 4th harmonic Nd:YAG laser, with 7 ns pulses of energy of
4.7 mJ and a source-probe separation of 5.1 mm.

Note that a positive displacement represents a displacement outward from the surface. In

order to determine the polarity of the PODS measurements with respect to surface

displacement, a sample was mounted in the sample holder and the oscilloscope signal

was monitored. By gently tapping the surface of the sample near the PODS probe spot, a

small deflection away from the PODS device could be generated. It was found that a

displacement as measured by the PODS as being negative is an inward surface

displacement, or a deflection away from the PODS device. As is characteristic of SAWs

generated in the ablative regime, the wave has a peak positive excursion, or crest, preceding a peak negative excursion, or valley, as the wave propagates outward. The theoretical model also predicts this polarity based on a symmetric cosine-squared spatial force distribution, which would be a reasonable approximation to a symmetric laser spot impacting on the target. This polarity is has also been measured by other researchers [12], [15], [35]. The ratio of the crest-to-valley amplitudes was found to be in the range of 0.2 to 0.6, which as will be shown later, is dependent on the source-to-probe separation and the spatial geometry of the laser spot. This is approximately consistent with the theoretical model calculations shown later for a symmetric force pulse, which predicts a crest-to-valley ratio of 0.55 assuming a symmetric spatial force profile, and no scattering or absorption of the SAW.

The SAW waveform also has a residual displacement after the SAW pulse with the surface of the material depressed inward by one to a few nanometers which will be discussed in the section 4.7. This agrees with the expected response to a Heaviside step function force applied to the target surface. Such a step function in pressure can be generated on the target surface from the blast wave in air generated by the laser plasma (which is discussed in Section 4.6), which lasts several microseconds after the plasma creation. The residual steps were generally small, on the order of a few nanometers, and are only a few times the single shot noise of approximately 1 nm RMS. The residual step displacement also scales with variation in laser energy, and distance between source and probe, which will be discussed later. Evidence of this residual step following the acoustic wave is also apparent in experimental SAW waveforms in previously reported publications [12], [17] though the step was not discussed explicitly in these references.

43

4.2 – Laser Intensity Dependence of SAW waveform

The amplitude of the SAW was observed to depend on the focal position of the lens, which affects the size of the spot and the resultant intensity. For this experiment a different focal spot geometry was employed than for the rest of the experiments. For the rest of the experiments, the KrF laser beam has a focal spot that is elongated horizontally with an asymmetric intensity profile in the horizontal direction. However, for the purpose of the present experiment, it was desirable to obtain a horizontally symmetric intensity profile. Two mirrors were aligned in such a manner as to rotate the spatial geometry of the KrF beam by 90°, thus making a more symmetric horizontal intensity profile and an asymmetric vertical intensity profile. The profile remained symmetric as the target was moved in front of or behind the best focal position, which was not the case for the normal beam orientation. Since the excitation and detection spots lie in the horizontal plane, the excitation spot profile will be symmetric in the direction of acoustic measurement. Therefore, as the focusing lens was moved in and out of focus, we could determine the acoustic amplitude as a function of focal position without effects of beam asymmetry. The measured peak-to-peak amplitude is plotted as a function of axial lens position in Fig. 4.2 where the relative axial position of best focus of the 75 mm focal length lens was defined as the 0 position. Since the spatial intensity profile of the KrF laser spot is symmetric, for equal plus or minus displacements from best focus, one would expect the measured acoustic response to be symmetric on either side of the best focus as is observed. It was also observed that the best focal position of the lens yielded a lower response than obtained at a position slightly out of focus. A position of 2 mm out of focus in either direction for the 75 mm lens gave the greatest acoustic response. The

44

acoustic response at these optimum intensities was ~1.5 times higher than at the best

focus conditions. Such behavior is expected since there is an optimum intensity for

which the coupling of impulse to the target is at a maximum [36]. The maximum

coupling of impulse for a given laser energy will in turn generate the maximum acoustic

response.
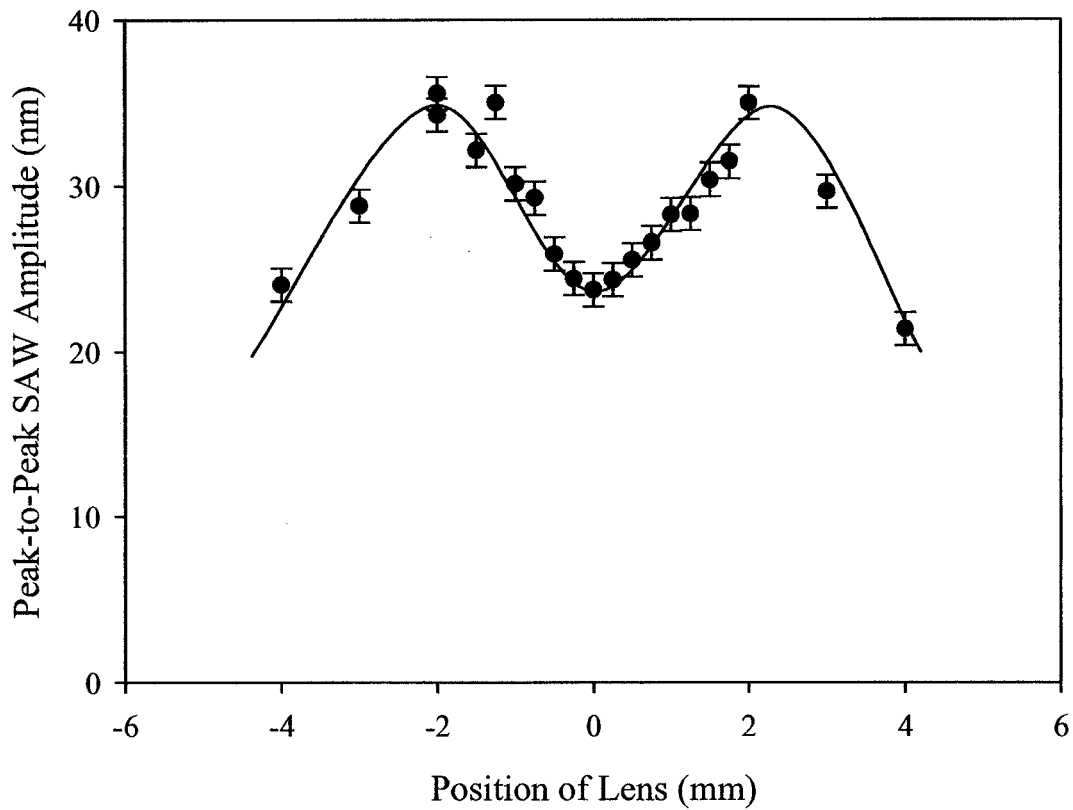
Fig. 4.2 – Dependence of the peak-to-peak SAW amplitude on the axial
position of the 75 mm focal length lens using KrF laser pulses, $E_L = 40$
mJ, $d_{probe} = 10$ mm. The solid line is a visual fit to guide the eye.

Due to the variation of KrF laser energy between approximately 35 mJ and 45 mJ per

laser pulse in the dataset used for Fig. 4.2, the peak-to-peak SAW amplitude was

normalized to a laser pulse energy of 40 mJ. This was done using a SAW amplitude to

laser pulse energy scaling law of $d_{nm} \propto E_{mJ}^{0.75}$, which will be discussed in the following section.

Since the spatial intensity profile corresponds to an equivalent effective temporal profile for the pulse generation, it is expected that a spatially asymmetric laser spot whose asymmetry inverts in passing through focus could produce an asymmetric response versus focal position. It would be expected that the peak-to-peak SAW amplitude produced on one side of focus would be larger than on the other side of focus. By using an asymmetric force pulses in the theoretical model calculations, one can show that both the crest-to-valley ratio and the peak-to-peak amplitude is affected by the geometry of the applied force pulse. A measurement taken without the rotation of the KrF laser focal spot, where such spatial asymmetry occurs, is shown in Fig. 4.3. In this case, the KrF laser has an asymmetric horizontal spatial intensity distribution and a clear asymmetry is observed both in the peak-to-peak SAW amplitude and the crest-to-valley ratio on the two sides of best focus, where again the relative axial position corresponding to best focus for the 75 mm focal length lens was defined as the 0 position.
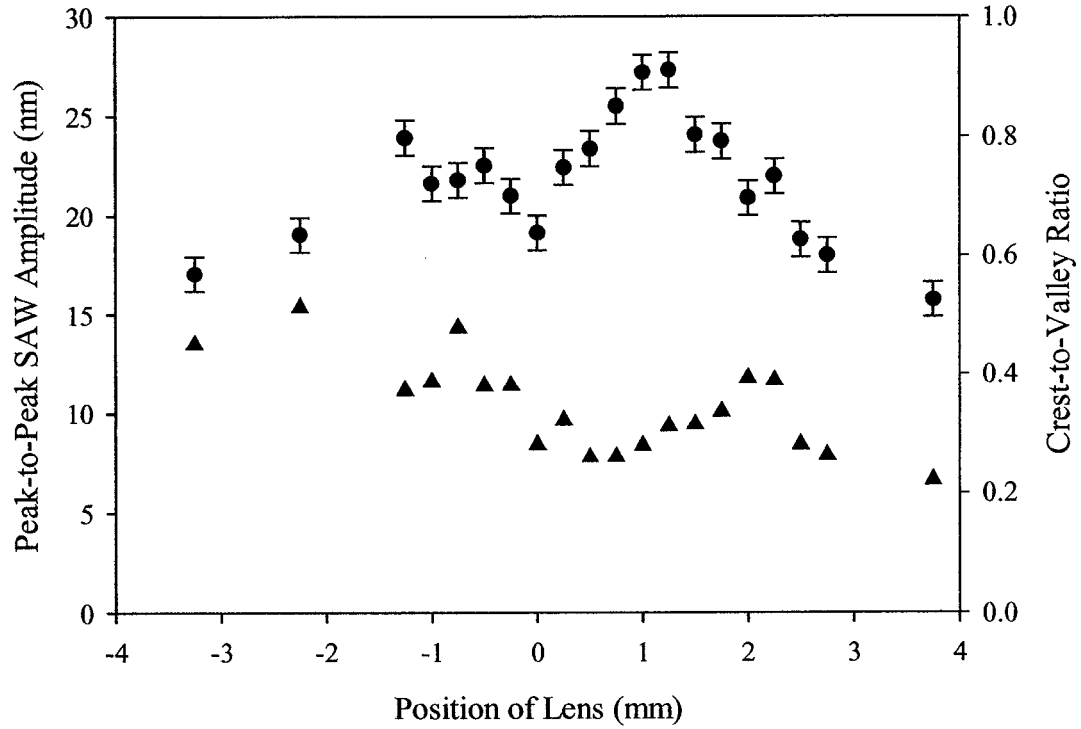
Fig. 4.3 - Dependence of the peak-to-peak SAW amplitude on the axial position of the 75 mm focal length lens using KrF laser pulses with asymmetric spatial intensity profiles. $E_L = 40$ mJ, $d_{probe} = 10$ mm. The circles are the peak-to-peak SAW amplitude and the triangles are the crest-to-valley ratio.

4.3 – Laser Energy Dependence of SAW Amplitude

The variation in SAW wave amplitude with laser energy was measured at probe distances of $d_{probe} = 6$ mm and 20 mm from the excitation point as shown in Fig. 4.4 (a) and (b). As various plasma pressure models have reported [18], [19], [37]-[39], the laser plasma pressure is expected to follow an intensity scaling power law in the range of $I^{0.75}$ to $I^{1.0}$, which for a fixed focal spot size corresponds to energy scaling laws of $E^{0.75}$ to $E^{1.0}$. An intensity scaling law of $I^{0.75}$ occurs in a strong plasma ablation regime and the $I^{1.0}$ scaling [18], [39] corresponds to the onset of the plasma ablation regime. The result

observed in the data shown in Fig. 4.4 (a) shows that for d_{probe} = 6 mm that a best fit for the 4th harmonic Nd:YAG laser pulses is given by a peak-to-peak amplitude scaling in nanometers of $3.1E_{mJ}{}^{0.71\pm0.05}$ nm and for the KrF laser measurements proportional to $2.2E_{mJ}{}^{0.73\pm0.06}$ nm where E_{mJ} is the laser energy in millijoules. The similar measurement for d_{probe} = 20 mm with KrF laser pulses gave a scaling proportional to $0.73E_{mJ}{}^{0.85\pm0.05}$ nm as in Fig. 4.4 (b). The observed scalings agree with the strong plasma ablation regime as would be expected for the intensities employed here. As shown in Fig. 4.4 (a), the peak-to-peak amplitude of the wave ranges from 2 to 43 nm in the energy range of 1 to 58 mJ. Note that the different focal conditions and different pulse lengths of the 4th harmonic Nd:YAG and the KrF laser pulses lead to a similar scaling law with a slightly different leading scale factor. The main reason for this is that for a given laser pulse energy, a smaller spot size yields a shorter duration acoustic pulse. Therefore the peak-to-peak amplitude must be larger to account for the similar total impulse delivered to the target. Since the impulse delivered to the target is a weak function of focal spot intensity (see Section 4.2), the 4th harmonic Nd:YAG laser at 1 mJ of laser energy for example, should yield a larger peak-to-peak SAW amplitude for the smaller 4th harmonic Nd:YAG laser spot on target than for a similar KrF laser pulse in a larger focal spot on the target. This is confirmed in the best fit energy scaling power law as in shown in Fig. 4.4 (a), where the leading coefficient in the case of the 4th harmonic Nd:YAG pulse energy scaling curve is 1.4 times larger than that of the leading coefficient for the KrF pulse energy scaling curve. This is also confirmed by the comparison of the horizontal crater size of 330 μm for KrF laser irradiation at 40 mJ pulse energy which is ~1.83 times larger than the 180 μm horizontal size of the 4th harmonic Nd:YAG laser produced crater at 5

mJ of pulse energy, and also by the time between the peak positive and peak negative excursions of the SAW, where the 140 ns time between peaks for the KrF laser generated SAW is 1.75 times larger that the 80 ns time between peaks for the 4th harmonic Nd:YAG laser generated SAW.
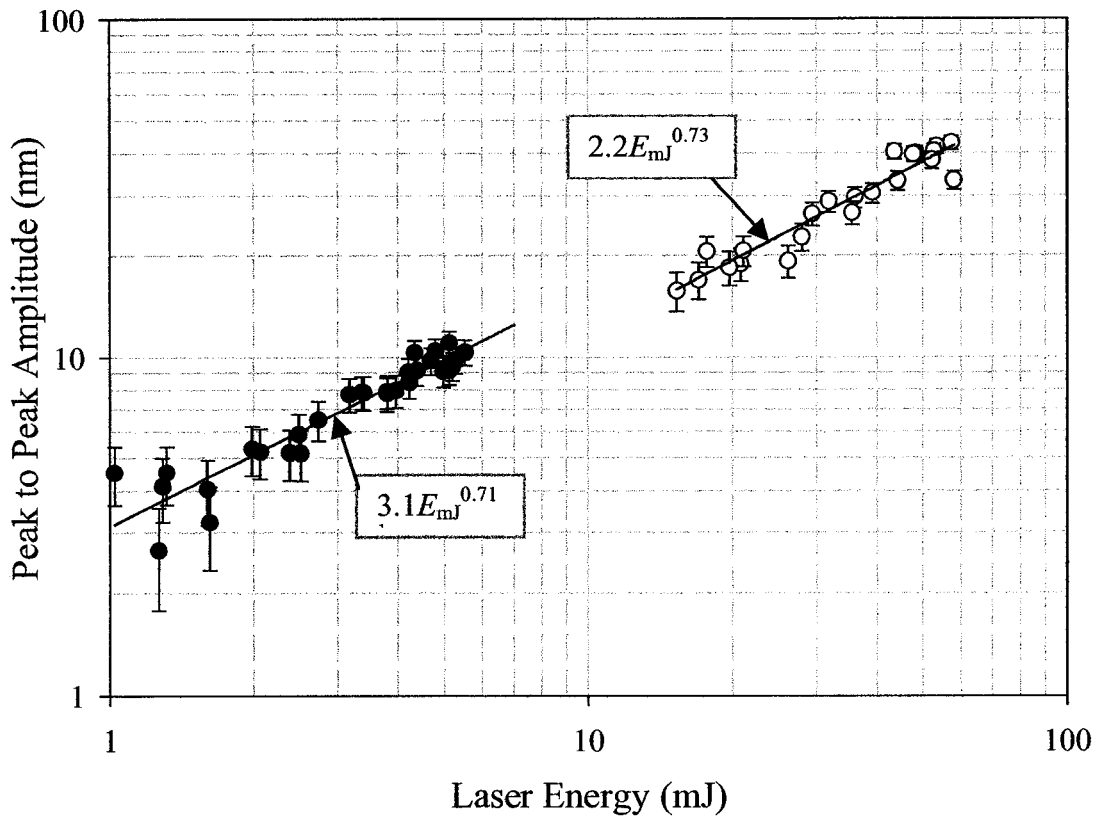
Fig. 4.4 (a) – Dependence of peak-to-peak SAW amplitude as a function of laser energy at 6 mm for KrF laser pulses (hollow) and 4ω Nd:YAG laser pulses (solid) at best focus. The solid curves are least squares power law fits to the data.
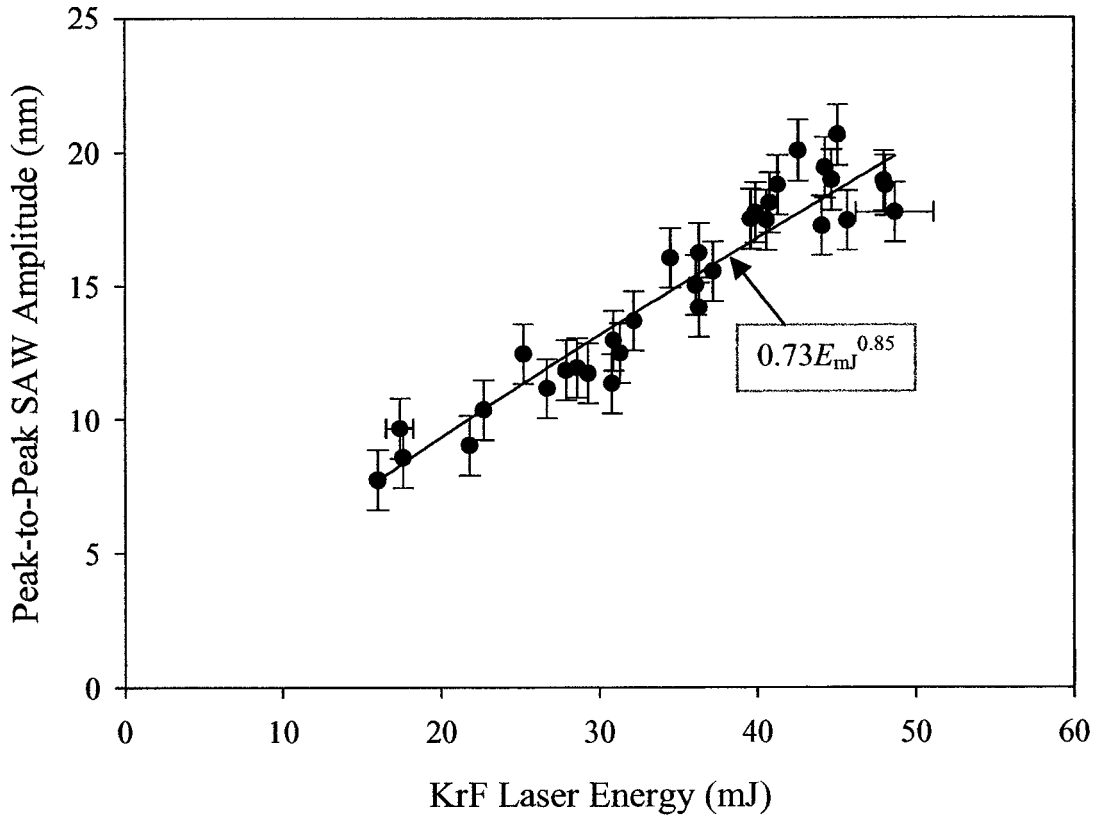
Fig. 4.4 (b) — Dependence of the peak-to-peak SAW amplitude as a function of KrF laser energy for a source-probe separation of 20 mm. The solid curve is a least squares power law fit to the data. The horizontal error bars are representative of those that would appear on all of the data points. The error in energy was estimated as ± 5% for the calorimeters used to measure the laser pulse energy.

4.4 – SAW Amplitude Dependence on Propagation Distance

Another important result is how the amplitude of the SAW depends on the distance between the probe and the excitation spot. This experiment was performed by varying the distance between the excitation spot and the probe spot. According to theoretical arguments, since the wave expands radially on the surface of the material, in the absence of dispersion, its intensity should vary inversely as the distance d_{probe} between the probe and excitation spot and thus the amplitude should vary as $d_{probe}^{-1/2}$ [40].

This functional dependence was approximately observed in the distance scaling measurements for aluminum shown in Fig. 4.5.
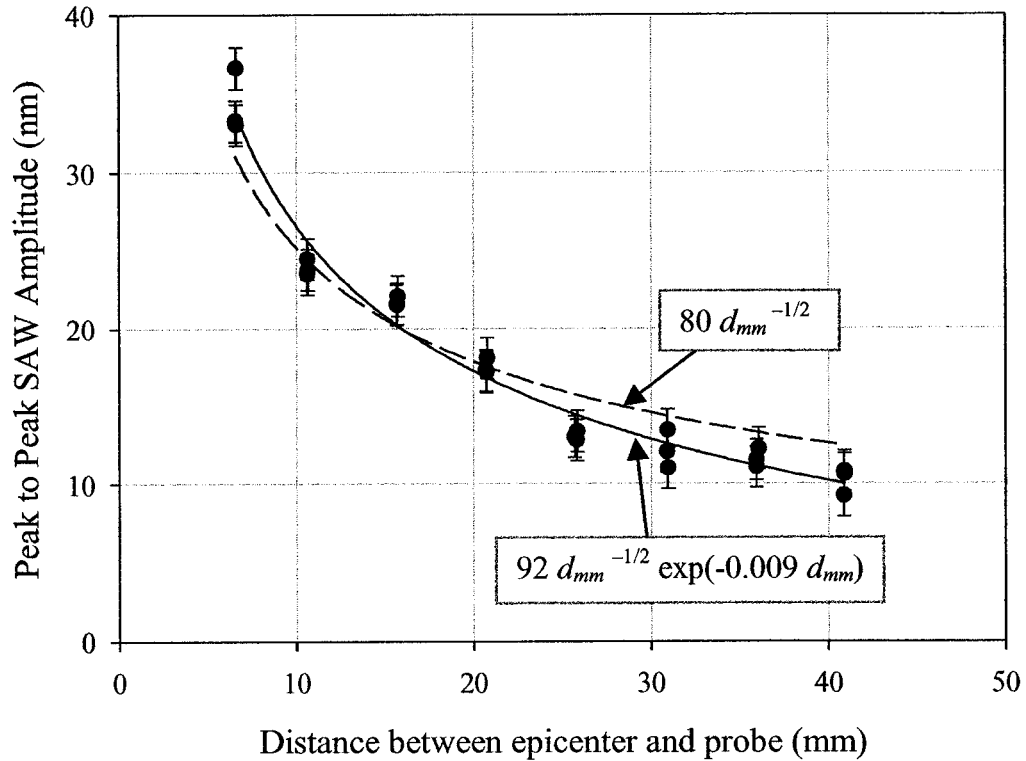
Fig. 4.5 – Dependence of peak-to-peak SAW amplitude as a function of distance between probe and excitation spot for a KrF laser energy of 40 mJ. The lines shown are least squares fit of a simple $d^{-1/2}$ power law curve (dashed) and a least squares fit including exponential decay of the signal due to absorption and scattering (solid). The probe distance, d_{mm}, is given in units of millimeters.

Note in Fig. 4.5 that the KrF laser was used, and since the energy of the laser varied over the course of the experiment in the range of 35 mJ to 55 mJ, the amplitude of the acoustic waves for each data point was normalized using an $E^{0.75}$ scaling law dependence to a laser energy of 40 mJ to reduce scatter in the data. This corresponds to the average of the energy scaling laws for the KrF laser pulses. As shown in Fig. 4.5, a best fit least squares scaling to propagation with attenuation is given by $92d_{mm}^{-1/2}\exp(-0.009d_{mm})$ nm where d_{mm} is the probe distance in millimeters. It is expected that random surface roughness

51

may lead to a shift of the center frequency due to the frequency dependent attenuation and damping of SAWs [41]. It has also been reported by other groups that microstructure and residual stresses in an optically flat surface will give rise to attenuation of SAWs [42].

De Billy *et al* [42] examined the attenuation coefficient for SAWs on duraluminum as a function of frequency. For an optically flat sample of duraluminum, an attenuation coefficient of 0.056 db/cm, or 0.000645 mm^{-1} for SAWs with a frequency of 2 MHz was obtained from their best-fit line to the data points (see Fig. 4 in [42]). Duraluminum is an obsolete term for a hard alloy of aluminum containing a copper, and magnesium, manganese, or silicon [43], [44]. It is very similar to the 6061 alloy of aluminum, which is composed of 97.9% Al, 0.6% Si, 0.28% Cu, 1% Mg, and 0.2% Cr. Their best-fit line is based on their own measurements, as well as a compilation of results reported by other authors. DeBilly's result on a plane surface is an order of magnitude lower than the result in this work of 0.009 mm^{-1}. The attenuation coefficient in DeBilly's work [42] was also measured for samples of varying roughness and predicts that an attenuation coefficient of 0.009 mm^{-1} for a 2 MHz SAW occurs for a sample roughness between 43 μm and 85 μm. Further study using samples of varying roughness is required to identify the cause of the present discrepancy.

Some modification, dispersion absorption or scattering, of the SAW appears to be confirmed by a change in pulse shape as evidenced by a variation in the crest-to-valley ratio as shown in Fig. 4.6 and by the variation in peak frequency of the SAW wave with the source-to-probe separation shown in Fig. 4.7. Since the frequency spectrum of the wave is changing with propagation, it is expected that dispersion is not the primary cause of the peak-to-peak amplitude decay. The change in pulse shape is indicative of

absorption or scattering of different frequency components in the SAW. This is consistent with the fact that the higher frequency components are decaying more strongly as the wave propagates, which would be expected for propagation along a surface with only small variations. It is also important to note however, that since the laser pulse energy varied during the course of this measurement, that the possible variation in the form of the source pulse may also be a factor in altering the frequency spectrum of the SAW waveform from shot to shot. Further study is required to clarify the change in pulse shape with propagation observed here.
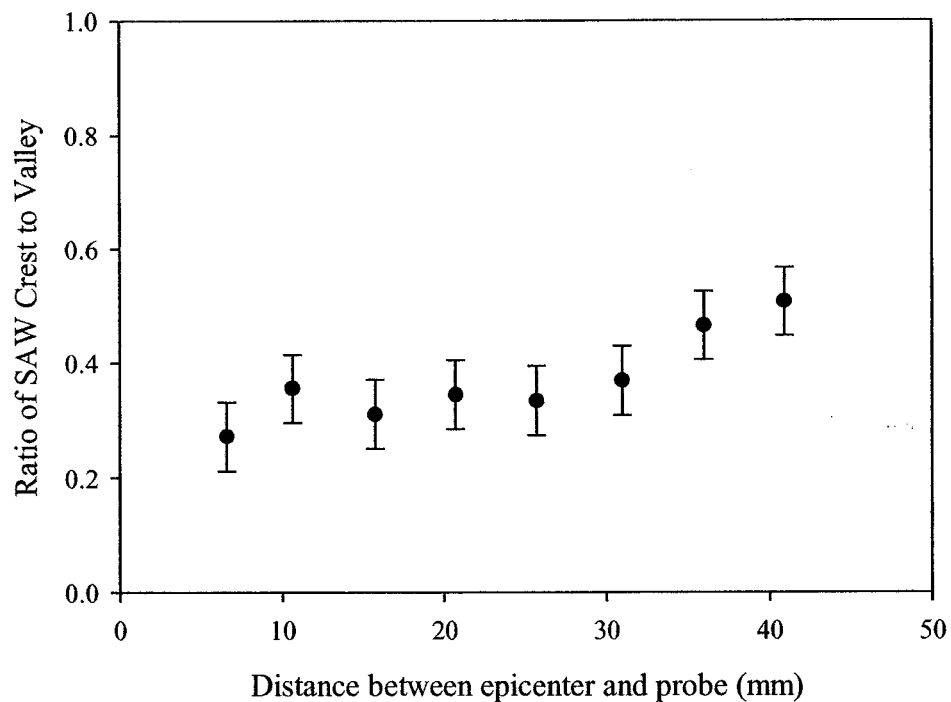
Fig. 4.6 – Dependence of the SAW Crest to Valley Ratio as a function of the distance between the epicenter and probe for the same data set as shown in Fig. 4.5.
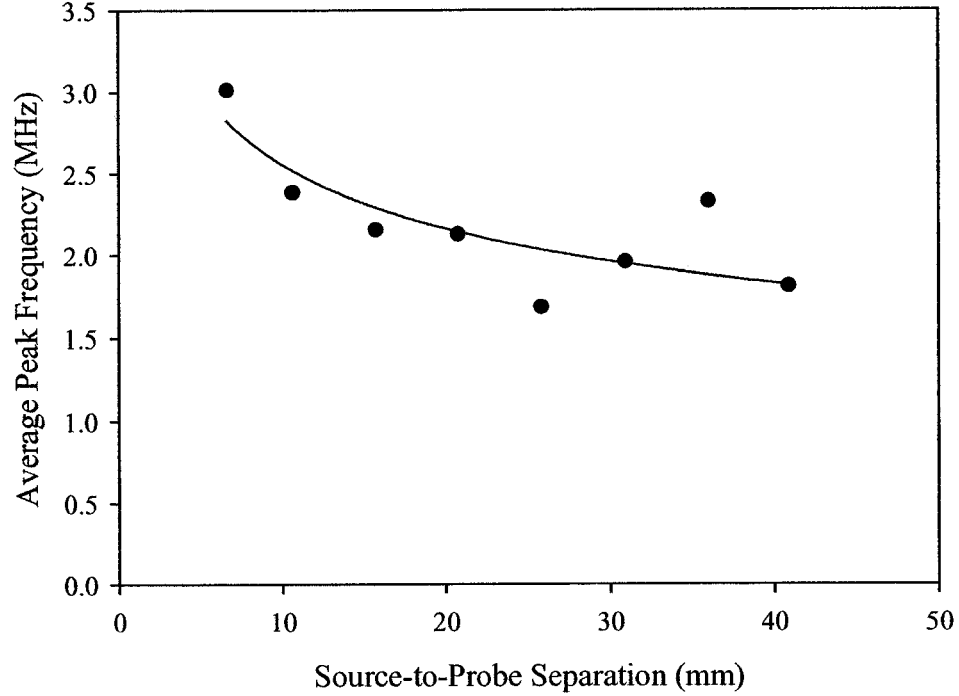
Fig. 4.7 – Dependence of the peak SAW frequency as a function of source-to-probe separation for the same data set as given in Fig. 4.5. Each data point is an average of the peak frequency for three SAW waveforms at each source-to-probe separation.

One method for counteracting the loss of SAW intensity as a function of propagation distance is to use a line source for excitation, rather than a point source [40]. The advantage to using this geometry is that the SAW amplitude no longer scales as approximately $d_{probe}^{-1/2}$, rather, within a distance less than the length of the line source, the SAW amplitude should remain approximately constant which has been shown for SAWs generated in the thermoelastic regime [40]. As d_{probe} approaches infinity, of course, the line source appears to be a point, and therefore the SAW amplitude would again scale as $d_{probe}^{-1/2}$. However, the available laser energy must be applied to a much larger surface area (line focus of several millimeters versus a single focal spot) and thus

the amplitude of the source excitation is reduced. Further experiments would be required

to establish the scaling of signals for the line focus spot geometry.

4.5 – Measurement of SAW Velocity in Aluminum

The acoustic pulse propagation times measured as a function of distance are

shown in Fig. 4.8. The time delay is measured from the peak of the laser pulse to the

time of the zero intercept between the crest and valley of the SAW and has been

corrected for all signal propagation delays in the instrumentation.

Distance between epicenter and probe (mm)
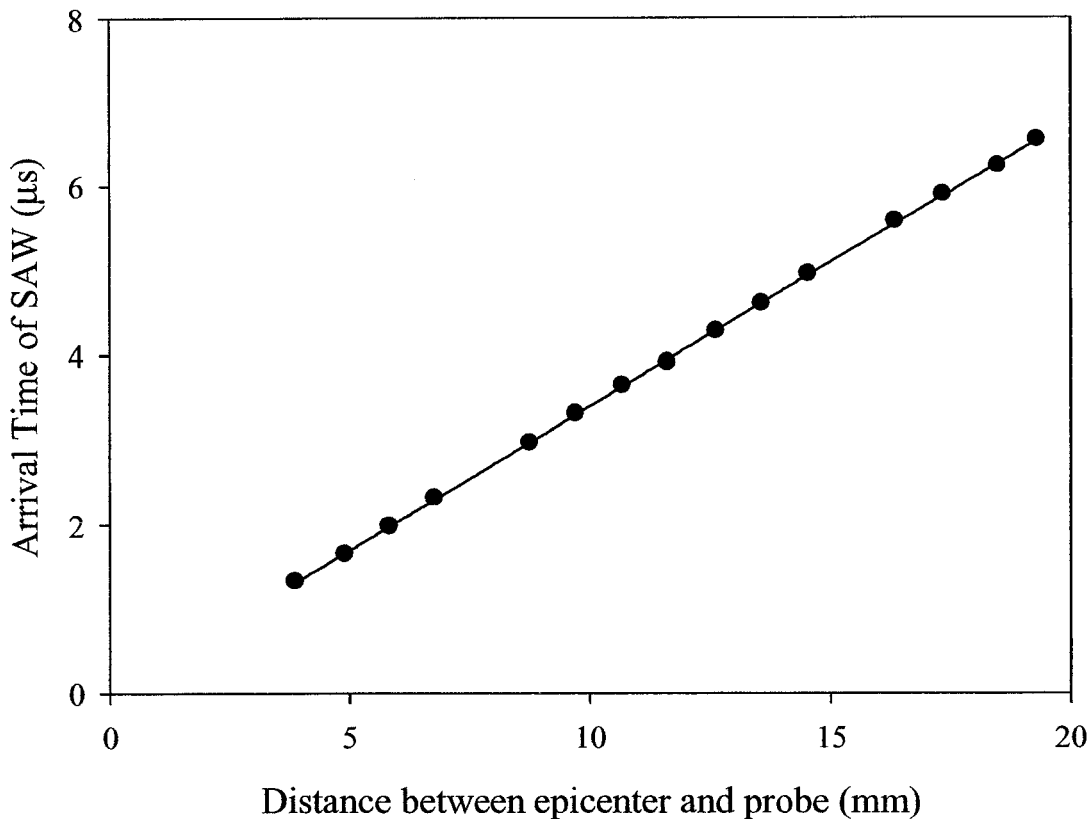
Fig. 4.8 – Measurement of SAW velocity of Al 6061, where a least
squares fit yields an acoustic velocity of 2937 ± 4 m/s constrained to
intercept the origin. Arrival time of the SAW is defined as the time
duration from the peak of the laser pulse hitting the target to the point
of zero crossing between the crest and valley of the SAW. The 4th
harmonic Nd:YAG laser was used for these measurements.

As can be seen, no detectable variation in the group velocity appears to occur due to any potential acoustic attenuation. Fitting a least squares linear curve constrained to have a zero intercept to these data points yields a SAW velocity in this sample of 2937 ± 4 ms^{-1}. The distances in this particular experiment were accurately measured by translating the sample after each laser shot using a micrometer stage to position the ablation crater directly under the PODS probe spot. By doing this, we could determine the distance between probe and excitation spot to ± 0.05 mm precision. Thus, as shown, using multiple shots at a number of distances, the acoustic velocity can be determined to a high degree of precision of 0.14%. For single shots taken at a distance of 15 mm, the acoustic velocity can be measured to within a standard deviation of ~0.4% based on the observed standard deviation for the propagation times of 20 ns from the best fit curve. This degree of precision agrees favorably with previously reported results on acoustic speed measurements on Al_2O_3-Al-SiC, PZT, and Germanium [2], which indicated accuracies of $\pm$ 0.1% to $\pm$ 1% could be obtained. Using more accurate measurements for distance, which was mainly limited by the crater size in the present experiment, and finer digitization time steps of 5 ns or less, it is expected that one could achieve an even more accurate determination of acoustic speed. Such accurate velocity measurements can easily distinguish several metals apart (e.g. aluminum c_R = 2940 ms^{-1} [1], mild steel c_R = 3000 ms^{-1} [1], rolled copper c_R = 2130 ms^{-1} [45] (based on values given for c_p and c_s and Eqn. 2.6), and nickel = 2800 ms^{-1} [45] (based on values given for c_p and c_s and Eqn. 2.6)) and be used as an indicator of metallic composition of samples.

4.6 – The Plasma Produced Blast Wave in Air

Several microseconds after the appearance of the SAW, evidence of the supersonic blast wave in air appears in the dataset. The blast wave in air is detected due to the change in the index of refraction in air, which in itself is not a displacement. However, the change in index of refraction changes the optical path length to the sample surface and thus the blast wave is seen as an apparent displacement of the surface.

As has been shown [46]-[48], a plasma-produced blast wave in air is composed of an outward leading front of high density relative to ambient density, followed by a relative low density inner region. The change in optical path length described by a region of density of length d, normal to the sample beam propagation direction is described by [49]:

$$\Delta = 2d(n - n_0) \qquad (4.1)$$

where Δ is the change in optical path length, d is the thickness of the constant density region, n_0 is the ambient index of refraction, and n is the index of refraction of the constant density region. Note that in the present case, the factor of 2 comes in since the measurement beam is reflected back through the higher density region.

However, this is for measurement through a constant density region. In the real experiment, the density relative to ambient air and therefore index of refraction change is variable throughout the blast wave, and evolves as the blast wave expands and weakens as a function of time. Another issue is that the index is measured through a chord of the sphere containing various densities, as is illustrated by Fig. 4.9:
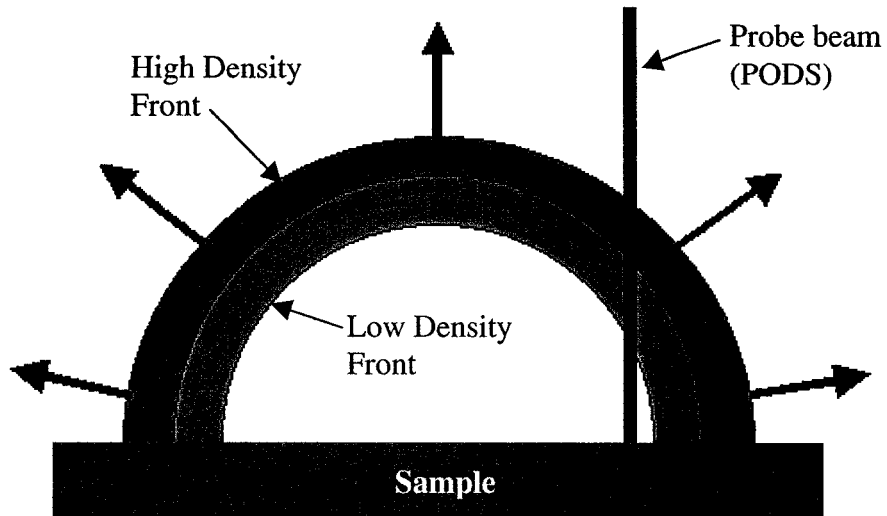
Fig. 4.9 – Illustration of the measurement scheme for the radially expanding blast wave in air.

Since the measurement is made through a variable density profile, the general form for Eqn. 4.1 in this case is:

$$\Delta = 2\int_0^D (n(z) - n_0)dz \qquad (4.2)$$

where $n(z)$ is the index of refraction profile along the probe beam propagation axis, z, and D is the total distance from the PODS aperture to the sample.

An example of the interferometer measurement of the blast wave in air is shown in Fig. 4.10:
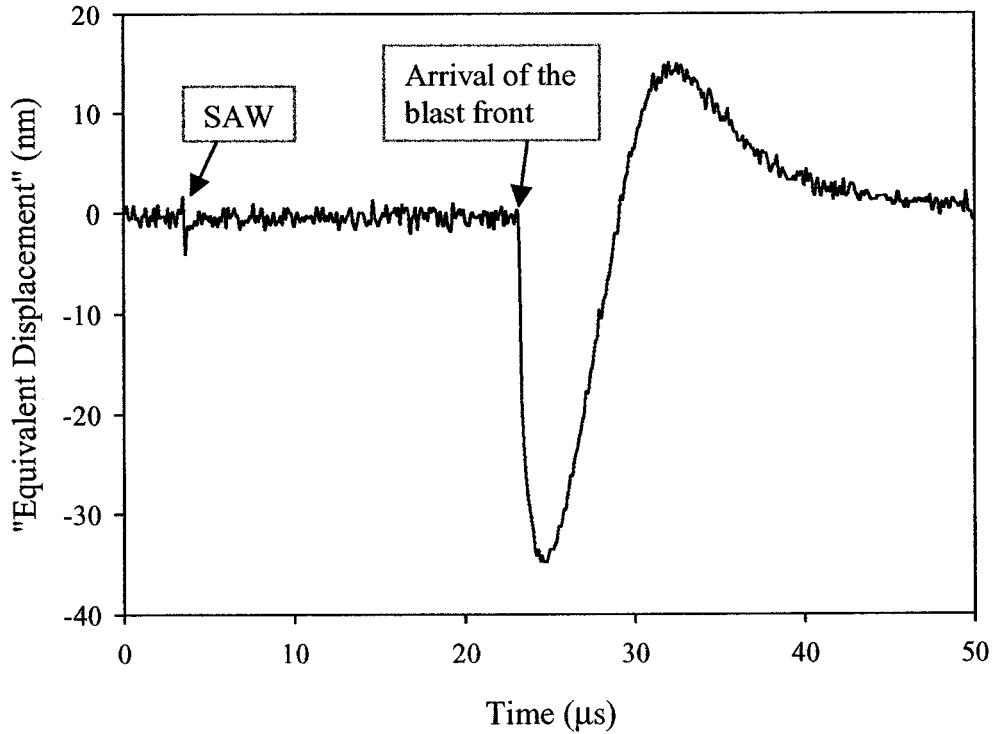
Fig. 4.10 – Blast wave in air occurring several microseconds after the SAW as detected by the PODS device as an equivalent displacement for a 4th harmonic Nd:YAG laser pulse energy of $E_L = 5.7$ mJ, and a source-probe distance of 10 mm.

Note in Fig. 4.10 that the blast wave in air for this particular case arrives approximately 20 microseconds after the arrival of the SAW. From Fig. 4.9, it can be seen that there is a region of high density relative to ambient followed by a region of low density relative to ambient. This corresponds to a peak negative apparent displacement as in Fig. 4.10 followed by a peak positive displacement.

Preliminary results indicate that the peak negative apparent displacement amplitude scales with the laser pulse energy, as well as inversely with the source-to-probe distance. Also, the arrival time of the blast wave as defined by the time between the laser pulse and the leading edge of the blast wave also scales as a function of the laser pulse energy for a fixed source-to-probe distance, and as a function of source-to-probe distance

for a fixed laser pulse energy. An example of this is the scaling of the arrival time of the leading edge of the blast wave with 4th harmonic Nd:YAG laser pulse energy, which is shown in Fig. 4.11:
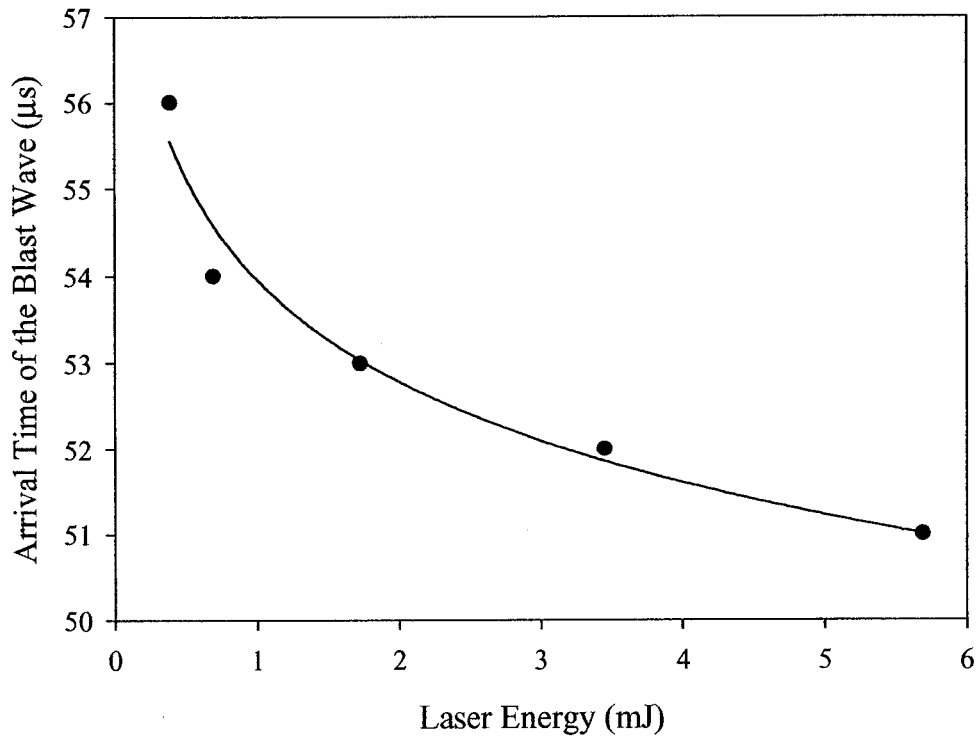
Fig. 4.11 – Arrival time of the leading edge of the blast wave in air as a function of 4th harmonic Nd:YAG laser pulse energy for a source-to-probe separation of 20 mm. The curve is a visual fit to guide the eye.

As can be seen, the wave travels supersonically for a longer period of time at higher laser energies, and as the laser energy is decreased the blast wave arrival corresponds to a speed approaching the linear acoustic speed in air, which is an arrival time of 58.3 μs for a source-to-probe separation of 20 mm, and an acoustic speed of 343 m/s at 20 °C. Further work is required to accurately quantify the expected scalings. These parameter dependencies indicate that the measurement of the blast wave in air can be a useful calibration check, for example, in verifying the energy deposited into the plasma (and therefore the laser pulse energy) and the source-to-probe distance.

60

4.7 – The Residual Step Displacement

Directly following the appearance of the SAW, a residual step in the relative surface displacement of the sample was measured, which was highlighted in Fig. 4.1. The appearance of the step displacement after the main SAW pulse was attributed to the downward surface pressure caused by the blast wave in air as was discussed in Chapter 4.6. Let us first examine the laser energy dependence on the amplitude of the post pulse residual displacement. The step was measured by averaging several data points for a source-to-probe distance of 20 mm. The results for the experiment are plotted in Fig. 4.12.
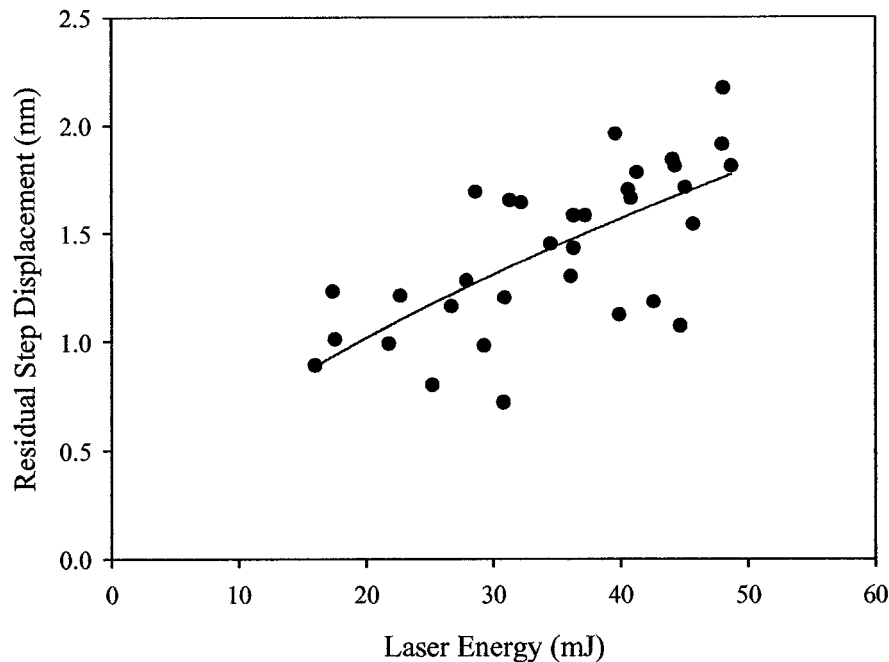
Fig. 4.12 – The residual step displacement in the tail of the SAW pulse plotted as a function of laser energy for a source-to-probe separation of 20 mm. The line is a best-fit power law to the data points. Measurements were carried out using a KrF laser pulse at best focus.

There is a large amount of scatter in the data. Despite this, there is a trend towards larger step displacements as the laser pulse energy increases. The least squares best power law

fit to this data gives a step displacement given by $d_{step} = 0.15\ E_{mJ}^{0.6 \pm 0.1}$ [nm]. This proportionality is qualitatively consistent with measured energy dependence for the peak-to-peak SAW amplitude, which was shown in Fig. 4.4.

The displacement of the residual step is also dependent on the source-probe distance. The step was examined in a similar fashion for the data set that was shown in Fig. 4.5. This dependence is given in Fig. 4.13.
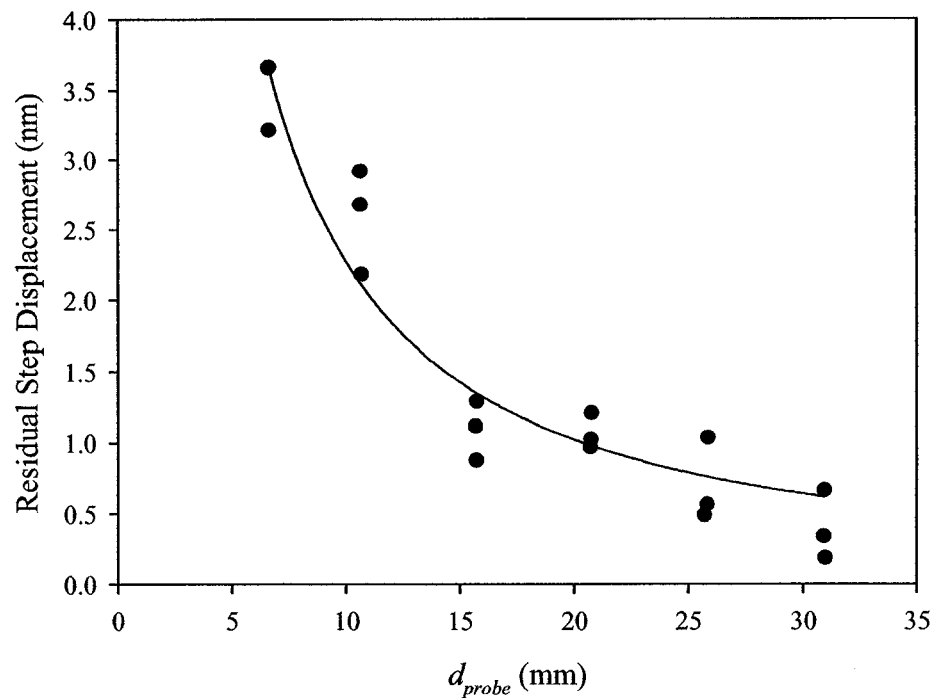
Fig. 4.13 – The residual step displacement as a function of the source-probe distance for a KrF laser energy normalized to 40 mJ. The line is a best-fit power law.

The dependence of the residual step on the source-probe distance follows a least squares best fit power scaling law of $d_{step} = 33\ d_{probe}^{-1.2 \pm 0.1}$ [nm]. This result is not consistent with the scaling of the peak-to-peak SAW amplitude as a function the source-to-probe distance. However, since the residual step is believed to be due to the normal surface force produced by the time dependent expanding blast wave, it cannot be

compared directly to the observed scalings of the peak-to-peak SAW amplitude. In order to quantify the expected scaling of the residual step displacement, further study on the blast wave solution, which in this case undergoes a transition between the strong and weak shock, is required.

Chapter 5 – Discussion[**]

In order to numerically model the experimental data, one must first extend the theoretical model to take into account the extended spatial extent of the excitation region in our experiment. In the model representation, the spatial point force can be extended spatially by modeling the experiment with many, spatially separated point forces that would occur over the whole spatial interaction region on the real sample, as is represented in Fig. 5.1. The surface acoustic wave excited at different positions in the focal spot will arrive at the observation point at different delay times. This can be modeled as an equivalent longer duration excitation force whose total impulse is equal to that of the original laser pulse.
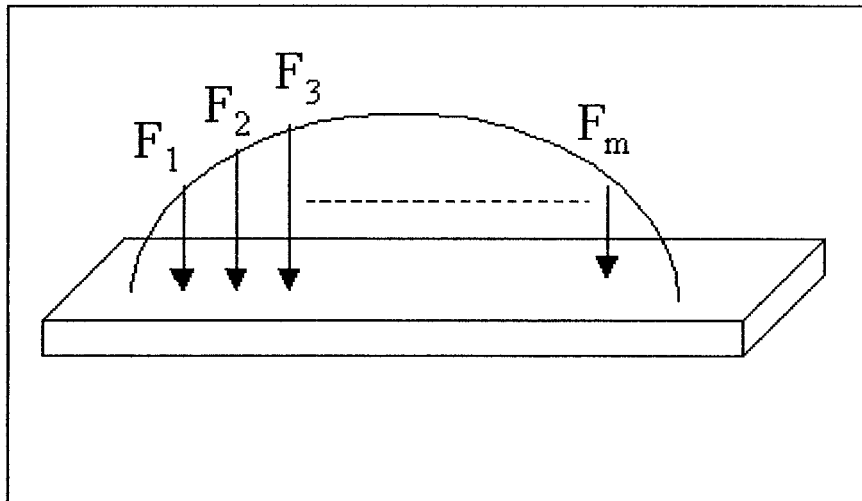
Fig. 5.1 – Illustration of many spatially separated force functions to model the resultant acoustic wave by using an equivalent temporal force profile to model a spatial force profile on the surface of the sample.

To illustrate this, it has been demonstrated that by choosing 18 equally spaced temporally separated force profiles of 10 ns FWHM equivalent spatial duration, each pulse delayed in time such that the FWHM time of interaction would be equivalent to a 206 μm spot on the surface of the aluminum sample, which is determined by the FWHM force pulse duration multiplied by the acoustic speed in aluminum of 2937 m/s, this would result in an equivalent spatial force profile as shown Fig. 5.2:
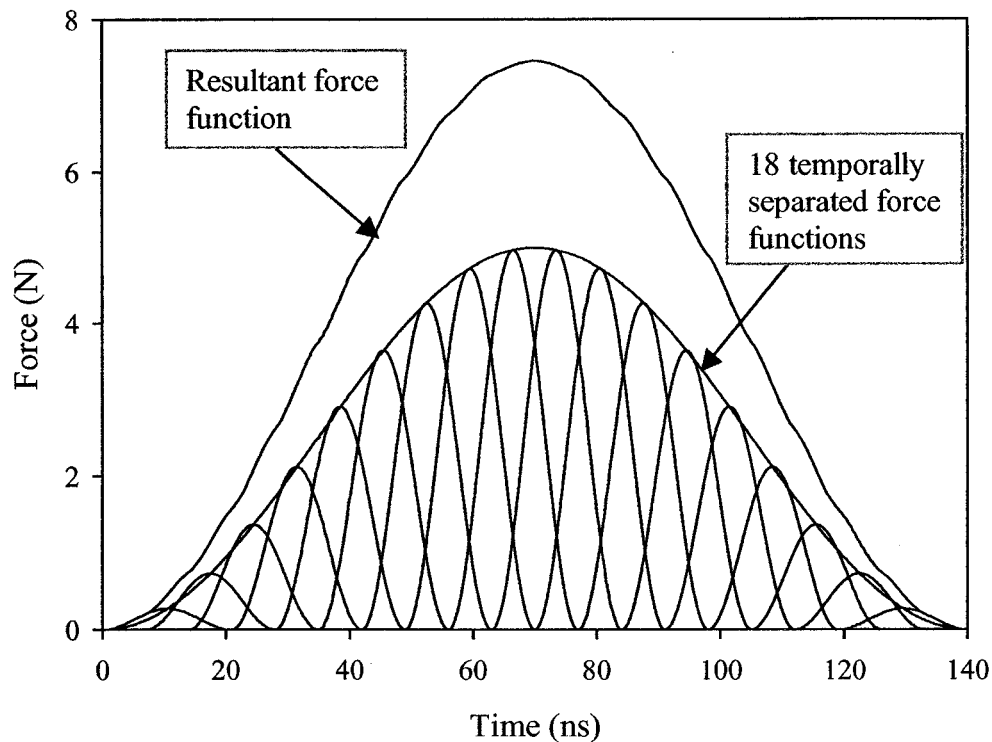
Fig. 5.2 – An equivalent summation of 18 spatially distributed force pulses of 10 ns FWHM duration. The total base-to-base envelope time duration in this case is 140 ns. The FWHM of the summation corresponds to a spatial size of 206 μm based on the SAW speed in aluminum.

Now by using separate 10 ns FWHM spatially separated force profiles and by applying the theoretical model as described in Chapter 2, 18 SAWs that correspond to the appropriate applied force would be obtained, each SAW slightly separated in time

according to the additional propagation time, as is shown in Fig. 5.3. Also shown in Fig. 5.3 is the resultant superposed SAW as a result of the summation of these 18 discrete SAWs.
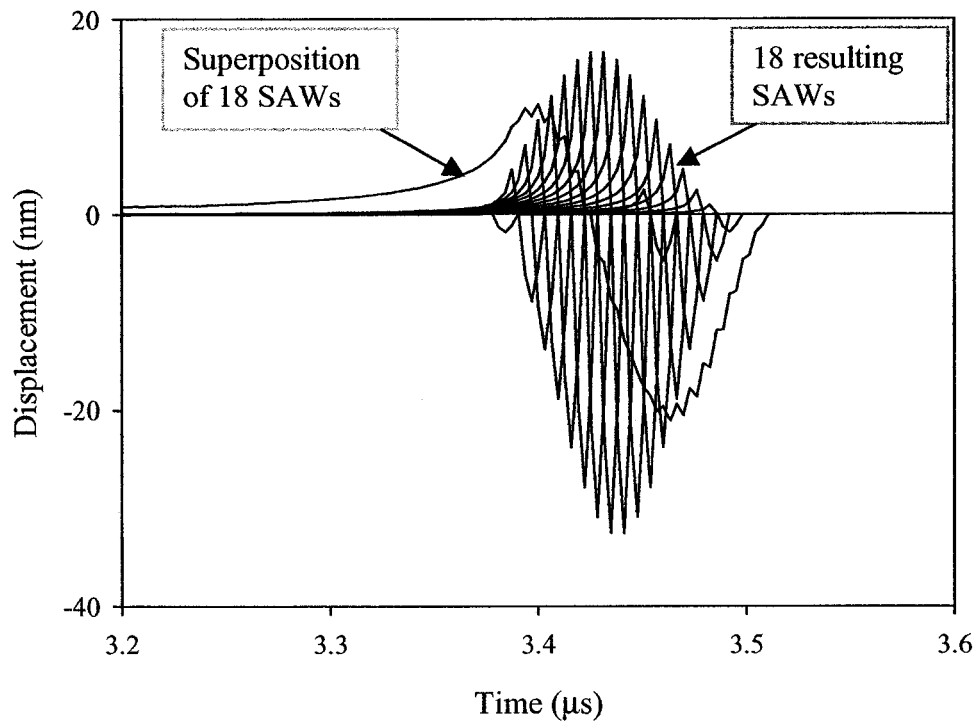
Fig. 5.3 — Resulting 18 SAW waveforms by using 18 spatially separated forces, and the resulting superposition of the 18 SAWs as a function of time.

Instead of the 18 individual force functions, a single 140 ns base-to-base cosine-squared function (Fig. 5.4) can be used as the applied force profile as described in Chapter 3. As can be seen in Fig. 5.5, the resultant SAW from the 140 ns base-to-base force profile compares well with the superposition of the 18 SAW profiles as was shown in Fig. 5.3.
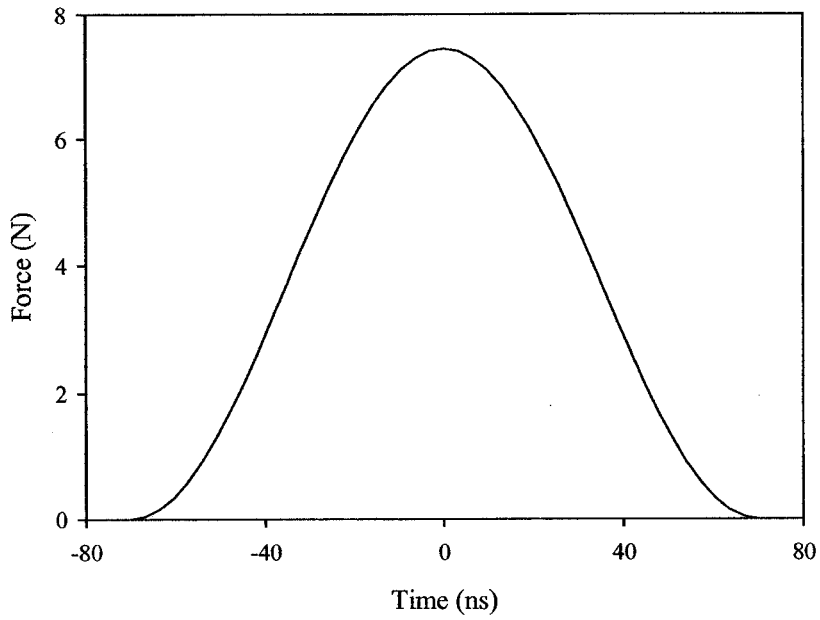
Fig. 5.4 – A cosine-squared applied force function with a base-to-base time duration of 140 ns.
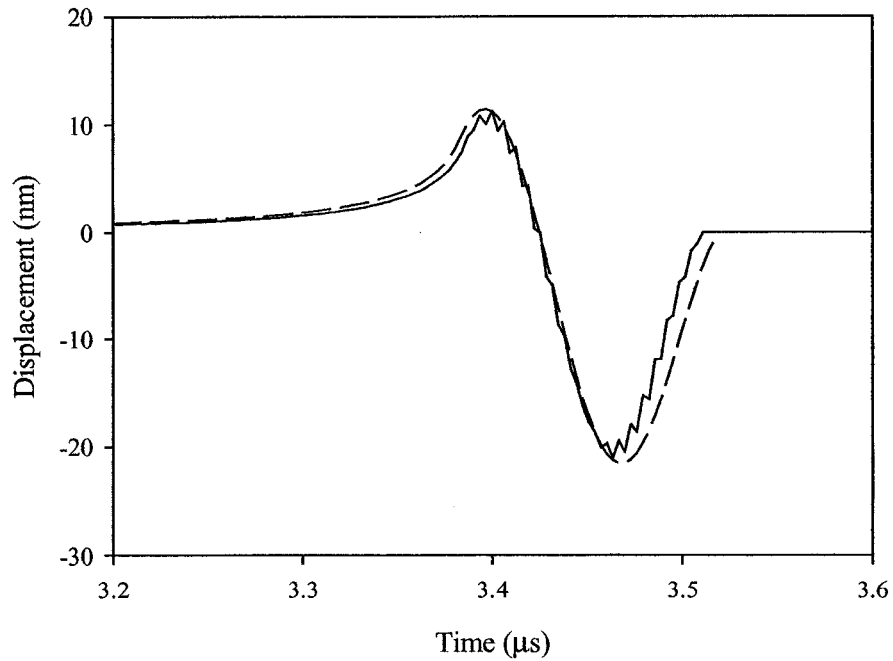
Fig. 5.5 – Comparison between the predicted SAW waveform by using a 140 ns base-to-base cos^2 force function (dashed) and the superposition of 18 SAWs generated using 20 ns base-to-base cos^2 force function spatially separated (solid). The peak force amplitudes are given in Fig. 5.4 and 5.2 respectively.

In this model, a longer pulse length was chosen, which accounts for the propagation time of the SAW across the excitation spot region given by approximately matching the full-width half maximum pulse duration of the excitation pulse given by Eqn. 5.1 to the laser spot size:

$$\frac{T}{2} = \frac{d_{spot}}{c_R} \qquad (5.1)$$

where c_R is the SAW velocity, d_{spot} is the effective excitation spot size in the direction of measurement and T is the base to base pulsewidth of a cosine-squared excitation pulse as given in Eqn. 5.1.

From comparisons to the measured waveforms an equivalent pulsewidth of $T = 225$ ns was used to fit the KrF laser generated SAW pulse data. This fit was found to give the most reasonable agreement to the waveform as an equally weighted average of two important parameters of the experimental waveform, that is, the time between the peak and valley of the pulse and the full-width at half minimum of the valley width, as illustrated in Fig. 5.6, which corresponded to theoretical force pulse durations of $T = 270$ ns and $T = 180$ ns respectively.
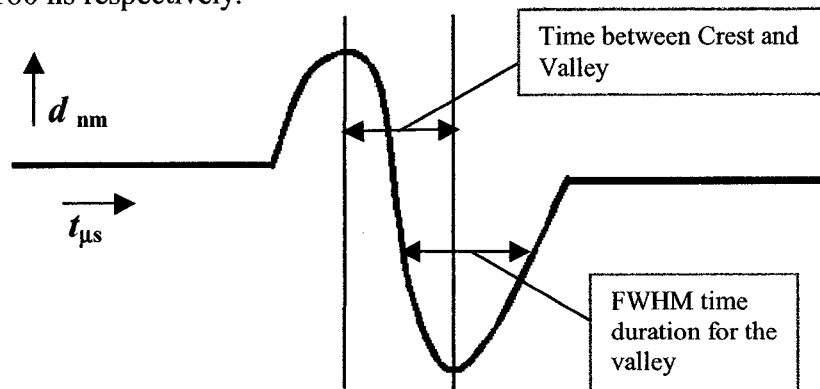
Fig. 5.6 – Illustration of a typical SAW to highlight the time between the Crest and Valley parameter, and the FWHM time duration of the valley parameter used to fit the model calculation of the SAW to the experimental SAW.

These values were determined by plotting the measured time between crest and valley and the FWHM time duration of the valley for the model SAWs as a function of the base-to-base time duration for the $\cos^2$ applied force as plotted in Fig. 5.7.
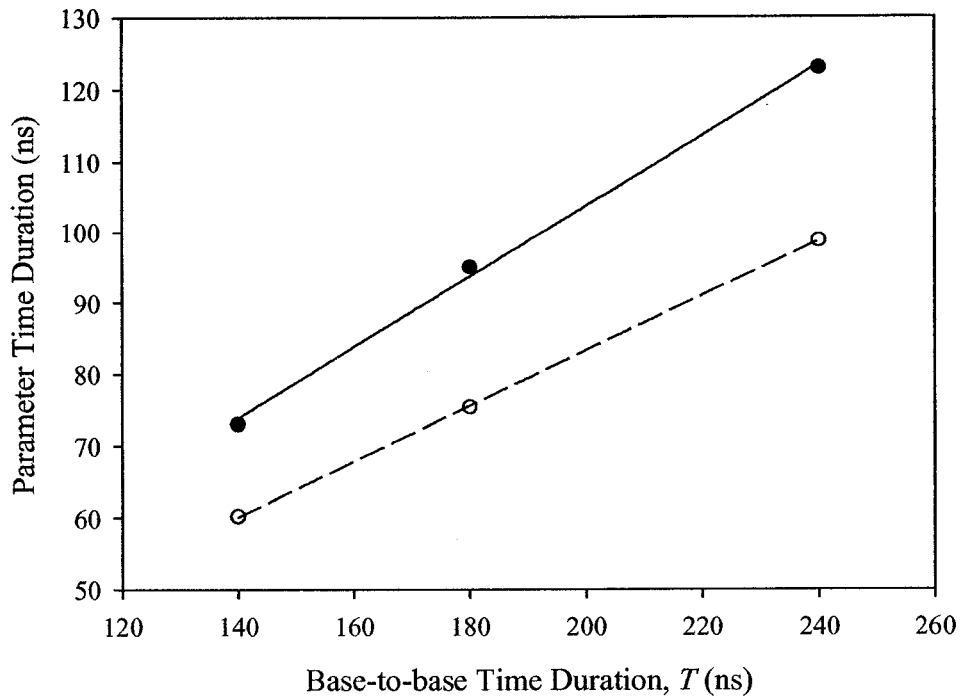
Fig. 5.7 – Time duration between crest and valley for the model SAW (solid) and valley FWHM for the model SAW (hollow) plotted as a function of base-to-base time duration for the cosine-squared applied force. The lines are best fit linear regressions to each respective data set.

The corresponding laser spot size according to Eqn. 5.1 would thus be 330 μm. This is larger than the actual 90% energy containing laser spot size of 210 μm in the direction of the measurement and is precisely the ablation crater size of 330 μm (shown in Fig. 3.12) at a laser pulse energy of approximately 40 mJ. The fact that the crater is much larger than the irradiation spot size is an indication of the strong shock wave, which is driven into the target by the laser pulse interaction. The shock wave continues to melt and blow off material for several 10's of nanoseconds after the laser pulse and thus acts

as the effective driving force source term, which will generate the surface acoustic wave. Even beyond the region of ablated material demarked by the crater, a strong shock continues to propagate for some distance as a nonlinear wave until it weakens into a linear acoustic wave. Only at that time does the linear Green's function method properly describe the acoustic wave. The nonlinear wave prior to this can be considered as the extended source term, which leads to the $T = 225$ ns (base-to-base) equivalent source pulse duration. For the 4th harmonic Nd:YAG laser pulse a reasonable fit to the data is given by using a pulsewidth of $T = 135$ ns which was determined by the same method as for the KrF laser case. From Eqn. 5.1 this corresponds to a $d_{spot} = 198$ μm. This is also very close to the crater size in this case of 176 μm (shown in Fig. 2.14) at approximately 5 mJ of laser pulse energy. Other researchers [15] have shown that the peak frequency and bandwidth of a thermoelastically-generated SAW is dependant on the laser spot size. Thus, for the ablative regime, the SAW pulse width should scale with the laser ablated region on the material.

In Fig. 5.8 and 5.9, experimentally measured and calculated SAW waveforms are shown at different probe distances for comparison. It should be noted that in Fig. 5.8 (a) and (b), the experimental distance d_{probe} was measured with a millimeter scale and not with the same precision as was done for the measurement of SAW velocity as in Fig. 4.8. For these cases, the arrival time of the theoretical waveforms have been adjusted to overlap the experimental waveforms. In Fig. 5.9 (a) and (b), d_{probe} was measured with a higher degree of precision (as was done for Fig. 4.8) and so neither the experimental nor theoretical waveforms have been shifted in time. The discrepancies in arrival time in Fig. 5.9 (a) and 5.9 (b) are due to the residual shot-to-shot inaccuracies in distance

measurement. The best fit values of F_{Pk} were determined by comparing to the experimental SAW waveforms generated for the two cases of the 4th harmonic Nd:YAG laser pulses and the KrF laser pulses. These comparisons were carried out for 40 mJ KrF laser pulses and 5 mJ 4th harmonic Nd:YAG laser pulses. The parameter values used for the case of aluminum were μ =26.1 GPa, ν = 0.34, c_p = 6400 ms^{-1}, and c_s = 3150 ms^{-1}, with the cosine-squared source pulse shape given by Eqn. 2.19. From fits to the SAWs produced by KrF and 4th harmonic Nd:YAG laser pulses, the average magnitude of F_{pk} was found to be equal to be 6.2 ± 0.4 N for T = 225 ns and 1.6 ± 0.1 N for T = 135 ns for the KrF and 4th harmonic Nd:YAG laser pulses respectively.
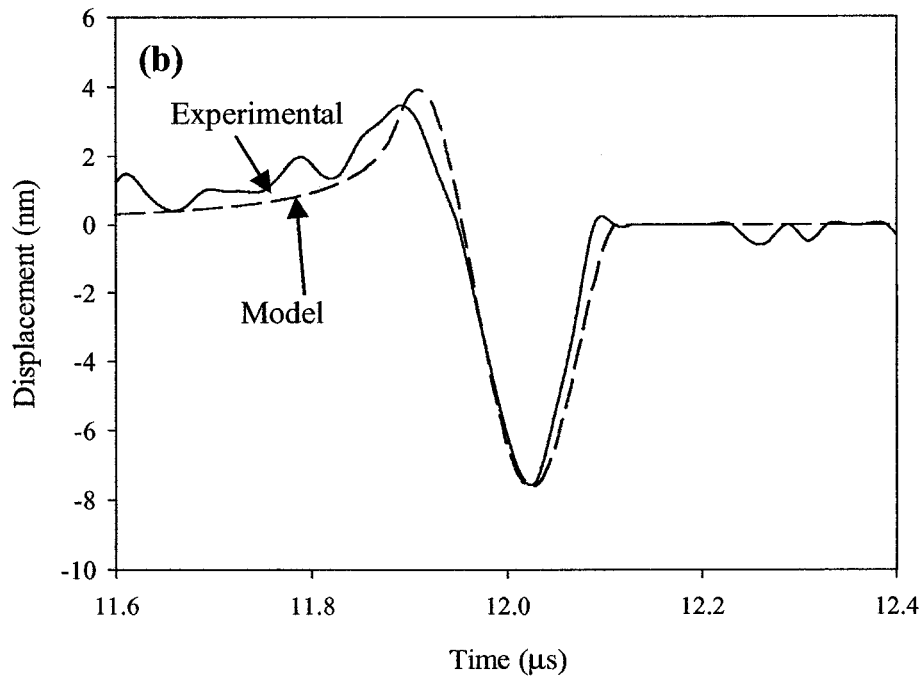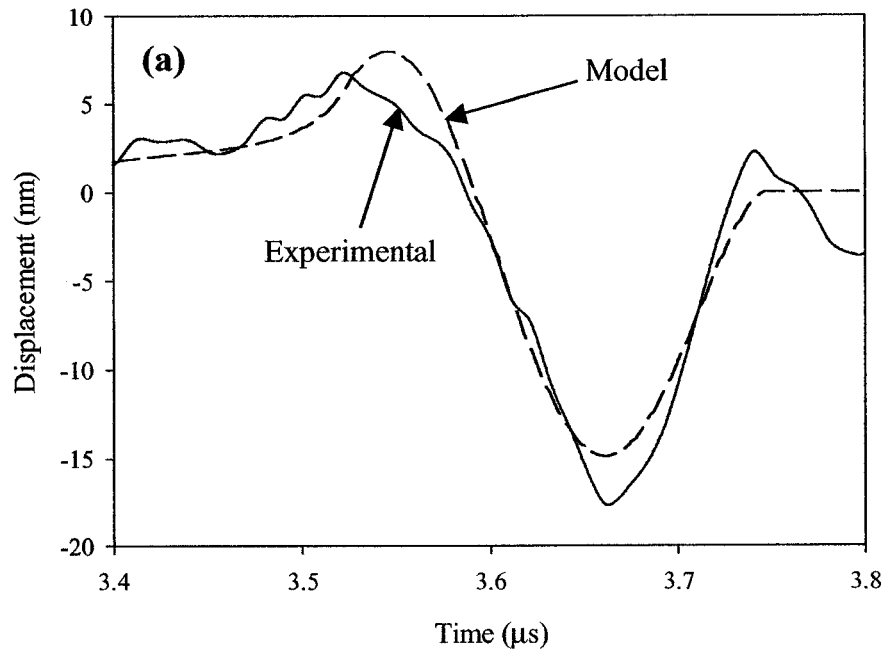
Fig. 5.8 – Experimental SAWs for a KrF laser pulse energy of 40 mJ as compared with theoretical waveforms using an excitation pulse of $T = 225$ ns and $F_{pk} = 6.2$ N for probe distances of (a) 10.6 mm and (b) 35.3 mm.
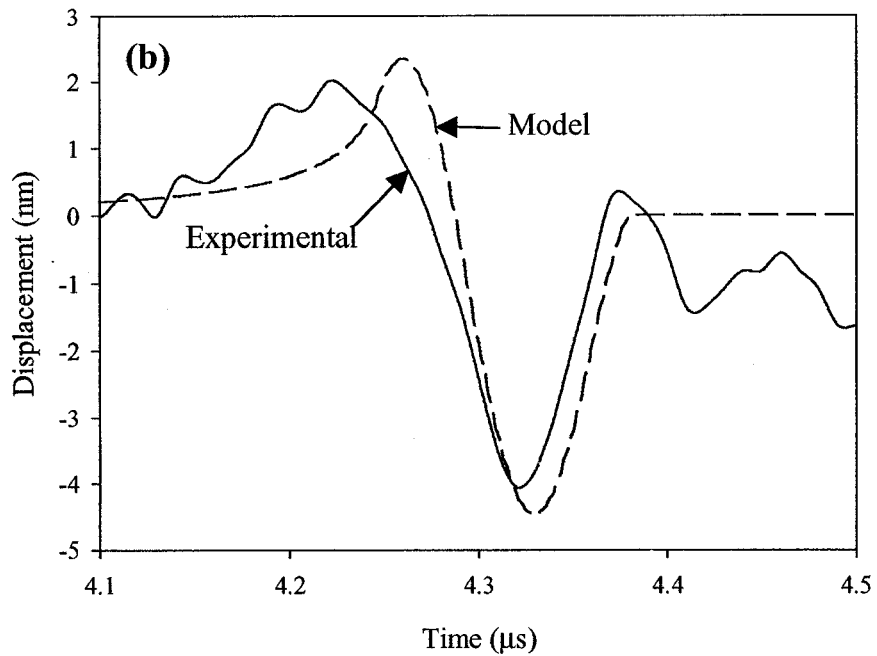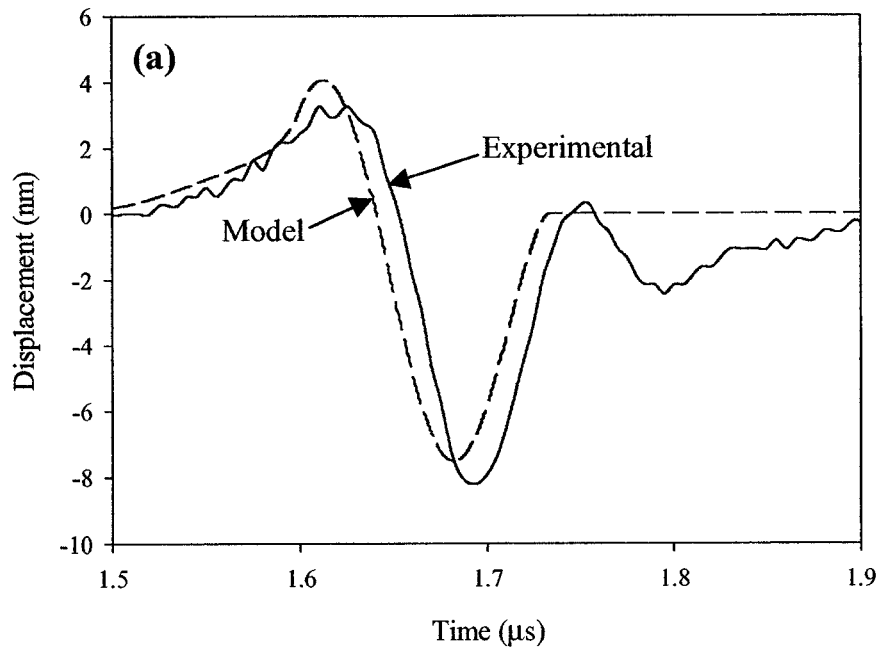
Fig. 5.9 – Experimental SAWs for a 4th harmonic Nd:YAG laser pulse energy of 5 mJ as compared with theoretical waveforms using an excitation pulse of $T = 135$ ns and $F_{pk} = 1.6$ N for probe distances of (a) 4.90 mm and (b) 12.62 mm.

For the generation of the surface acoustic waves the important parameter is the mechanical coupling of the laser pulse to the material as given by the impulse delivered to the target. From previous plasma scaling studies [18], [19], [36], the mechanical coupling coefficient can be defined as $C_m = P_{abl}/I = \int F(t)dt/E_L$, where I is the intensity of the laser spot, E_L is the energy of the laser pulse, and P_{abl} is the ablation pressure. This yields the impulse delivered to a target for a given laser pulse energy.

In [50], the self-regulating 1D plasma model was used to estimate the theoretical ablation pressure in the planar expansion case [19] yielding (see Section 2.2):

$$P_{abl} \approx 7.26 \times 10^8 \ I_9^{3/4} \lambda_{\mu m}^{-1/4} \tau_{ns}^{-1/8} \qquad \text{Pa} \qquad (5.2)$$

where I_9 is the intensity in units of 10^9 W/cm^2, $\lambda_{\mu m}$ is the wavelength of the laser in μm, and τ_{ns} is the FWHM pulsewidth of the laser in nanoseconds. This was based on estimates of $\ln \Lambda = 5$, and $Z' = 2$ (see Eqn. 2.15) for the low intensity laser produced plasma. Using the ablation pressure given by Eqn 5.2, one obtains a mechanical coupling coefficient of $C_m = 4.1 \times 10^{-5}$ NsJ^{-1} for a 40 mJ, 10 ns KrF laser pulse in a spot area of 3.1×10^{-4} cm^2. From this, we would calculate a total impulse of $\int F(t)dt = 1.6 \times 10^{-6}$ Ns. However, an iterative self-consistent calculation which determines $\ln \Lambda$ and Z' from the temperature and density of the heated plasma gives $\ln \Lambda = 3.6$ and $Z' = 4.8$ based on the predicted electron temperature of $T_e = 19.084$ eV and peak electron density of $n_e = 6.081 \times 10^{20}$ [51]. The Sesame Equation of State Database [51] was used to find Z'. Based on these new values, one obtains a mechanical coupling coefficient of $C_m = 2.771 \times 10^{-5}$ NsJ^{-1}. Thus, the expected total impulse is $\int F(t)dt = 1.11 \times 10^{-6}$ Ns based on this improved self-consistent calculation.

From experimental studies on ablation pressures in vacuum [36], a best fit curve for the mechanical coupling coefficient to a collection of published experimental data on aluminum has been reported as:

$$C_m = \frac{3.93 \times 10^{-5}}{\left(I_9 \lambda_{\mu m} \sqrt{\tau_{ns}}\right)^{0.301}} \qquad \frac{\text{Ns}}{\text{J}} \qquad (5.3)$$

Note, that this experimentally derived scaling law has a slightly different intensity scaling power law than the simple theoretical plasma model for which a power law of 0.25 is expected. The mechanical coupling coefficient here is approximately 1.4× lower than predicted above for an ideal simple plasma in the intensity range of interest. The slightly different scaling law and the factor of ~1.4× lower impulse is possibly due to the extra energy required to ionize the aluminum plasma and thermalize all the electrons created which leads to a larger nonlinear heat capacity for the real experiment than that used in the simplified theoretical derivation of the pressure scaling law given by Eqn. 2.15. Using the scaling law given by Eqn. 5.3 and the same parameters as in the previous calculation for the impulse, one would calculate a coupling coefficient of $C_m = 2.0 \times 10^{-5}$ NsJ^{-1}, which leads to an impulse of $\int F(t)dt = 7.8 \times 10^{-7}$ Ns for a 40 mJ KrF laser pulse.

This result is found to be in reasonable agreement with the values used in the theoretical modeling for a KrF laser pulse at 40 mJ, which would give an impulse of $\int F(t)dt = F_{Pk}\Delta \tau_{effective} = (6.2)(112.5 \times 10^{-9}) = 7.0 \times 10^{-7}$ Ns. This value is 63% of the impulse at best focus as predicted by the simple 1D plasma model [19] using the correct values for ln Λ and Z', and 90% of the predicted value at best focus based on the parametric scaling law given by Eqn. 5.3 [36].

Similarly, for the 4th harmonic Nd:YAG laser spot, the impulse predicted by the 1-D plasma model is 1.841×10^{-7} Ns [19] using $\ln \Lambda = 2.7$ and $Z^* = 4.8$ for a 5 mJ, 7 ns laser pulse, and 1.18×10^{-7} Ns based on the experimental derived scaling law [36] for a 7 ns laser pulse energy of 5 mJ. The impulse that was used to model the SAWs generated by the 4th harmonic Nd:YAG laser spot was 1.08×10^{-7} Ns. This is 59% of the value predicted by the 1-D plasma model, and 91% of the value predicted by the parametric scaling law given by Eqn. 5.3.

One can also employ a 3-D plasma model [19] to calculate the ablation pressure (see Eqn. 2.16) and the acoustic coupling from the spherically expanding plasma, using a scale length parameter, L, of 150 μm in the case of the KrF laser spot, and 100 μm in the case of the 4th harmonic Nd:YAG laser spot. These are estimated by the product of the ion acoustic velocity, $c_i = (k_B T_e / m_i)^{1/2}$ where k_B is Boltzmann's constant, T_e is the electron temperature in K, and the FWHM pulsewidth of the laser, τ. Thus the values for L in this case are approximately equal to the ablation crater radius for each laser spot. Using these values of L, one would determine that the pressure and acoustic coupling are within 1% of those predicted by the planar expansion model of the plasma. Thus in this case, the planar expansion and spherical expansion models agree in predicting the pressure and impulse delivered to the target.

It should be noted that the experimental intensity distribution for the KrF laser spot, as indicated by the CCD images of the laser spot, consists of a centralized hot spot of roughly gaussian distribution, with a larger low energy region surrounding the centralized hotspot and thus, the pressure pulse is not uniform over the whole surface. A second effect that is not accounted for in the above impulse scaling laws is the tamping

effect of air as compared to vacuum. One previous study [18] has shown that there is an ~20% increase (see figure 3 in ref. [18]) in the net impulse in air versus vacuum and thus it is expected that this should lead to an observed value higher than predicted. A final important factor may be the nonlinearity of the initial strong shock wave generated in the target by the plasma which may not couple to the excitation of the surface acoustic wave to the same extent as would be expected in linear theory. The inward propagating hemispherical shock wave carries a large amount of impulse into the target and perhaps leads to a decoupling of some of the energy that might otherwise be expected to launch the surface acoustic wave. This nonlinear regime of pulse generation is beyond the scope of the present treatment. Given all of these factors the agreement between experiment and theory is quite reasonable.

In comparing the results using two different lasers, the 4th harmonic Nd:YAG and the KrF laser, different pulsewidths are observed for the SAWs, with significantly shorter SAW pulsewidths for the case of SAW generation using the 4th harmonic Nd:YAG laser pulses. This agrees qualitatively with the fact that the laser focal spot size is almost twice as large for the KrF laser pulses compared to the 4th harmonic Nd:YAG. The concentration of the laser pressure impulse into a shorter acoustic pulse leads to the slightly larger amplitude of the pulses for the latter case as given by the scaling laws shown in Fig. 4.4. This is directly observed if one measures the time between the positive and negative peaks of the SAW which was measured to be 140 ± 10 ns for the KrF laser case and 80 ± 10 ns for the 4th harmonic Nd:YAG case. The concentration of similar impulses into a shorter acoustic pulse leads to the larger measured peak-to-peak amplitudes as given in Fig. 4.4.

As noted in the experimental results the largest amplitude acoustic waves are excited using irradiation at a position ±2 mm removed from best focus. Based on an assessment of published experimental work on aluminum in vacuum, an expression for the intensity at which maximum mechanical coupling occurs has been empirically derived [36], which for aluminum can be given by:

$$I_{max} \sqrt{\tau} = 8 \times 10^4 \qquad Ws^{1/2} cm^{-2} \qquad\qquad (5.4)$$

This intensity for maximum mechanical coupling efficiency represents the transition from a weak ablation to a strong fully ionized plasma ablation regime. From this, one may predict an intensity for maximum coupling of 8×10^8 Wcm^{-2} for a 10 ns KrF laser pulse. The 90% energy containing area as measured by the CCD camera at a position 2 mm out of focus was 8.7×10^{-4} cm^2, which for a laser energy of 40 mJ and duration of 10 ns gives an average intensity of 4.1×10^9 Wcm^{-2}. Thus while the occurrence of an intensity leading to optimum excitation of an acoustic wave is observed, the observed optimum coupling intensity is approximately five times higher than the empirical scaling law given by Eqn. 5.4. However it should be noted that the data used to derive the scaling law given in Eqn. 5.4 incorporated lasers with many different wavelengths and focal spot conditions and are scattered over a band a factor of 10 wide on the logarithmic intensity scale of Fig. 2 of reference [36]. Thus the present discrepancy may not be unreasonable given the degree of scatter of many different experiments from this scaling law. Comparing the intensities of 4.1×10^9 Wcm^{-2} at 2 mm out of focus versus 1.2×10^{10} Wcm^{-2} at best focus for the case of 40 mJ KrF laser pulses, an increased impulse of 1.33 times would be predicted for the optimum out of focus position according to the pure plasma scaling model given by Eqn. 5.2 or 1.42 times given by the empirical model given by Eqn. 5.3. This is in reasonable

agreement with the results in Fig. 4.2 where the amplitude of the acoustic wave is ~1.5 times as strong at 2 mm out of focus as compared with the acoustic pulse at best focus. It is expected that other variables such as ratio of laser spot diameter to hot plasma expansion diameter and maximum shock wave expansion diameter will also be important in this scaling. Further study will be required in order to clarify the details of the observed behavior.

The result obtained for the SAW velocity of 2937 ± 4 ms^{-1} can be compared to previous reported values. Scruby and Drain [1] give a value of $c_R = 2940$ ms^{-1} for aluminum. Neubrand [52] reported a SAW velocity of 2934 ms^{-1} for pure aluminum. Doyle and Scala [40] used a Rayleigh wave slowness to model results measured on the 7076-T6 alloy of aluminum of $s_R = 0.341$ s km^{-1}, where the Rayleigh slowness is c_R^{-1}. This translates to a SAW velocity of 2930 ms^{-1}. Thus the measured velocity is in good agreement with past values reported for aluminum.

Finally, comparisons can be made with previously reported quantitative measurements of SAW amplitudes generated in the thermoelastic and ablative regimes. For the thermoelastic regime, for a line geometry laser spot on aluminum, a peak-to-peak amplitude of 370 pm was measured [40] for source-to-probe separations much less than the length of the line. The laser used was a Nd:YAG laser with an average pulsed energy of 2.9 mJ, with an FWHM pulse duration of 25 ns. The spot geometry was a line with a 20 mm length and a < 30 μm width. Scruby *et al* [12] also found that the peak-to-peak SAW amplitude in the thermoelastic regime varied linearly with the laser pulse energy, up to a peak-to-peak SAW amplitude of 44 pm for a circular spot source well out of focus with a Nd:YAG laser pulse energy of 20 mJ. Two previous studies have reported on

quantitative measurements of ablatively driven surface acoustic waves from point source excitation. The first study used the fundamental frequency of a Nd:YAG laser with an energy of 80 mJ per pulse and a pulse duration of ~30 ns [16]. The second study, also used a Nd:YAG laser with 25 mJ of energy at the fundamental frequency, and a 30 ns FWHM pulse duration [17]. In the first study, the $d_{probe}^{-1/2}$ dependence in amplitude as a function of distance d_{probe} on a polished steel block was reported, with a 6.4 nm and 2.1 nm peak-to-peak amplitudes for distances of 1.3 mm and 13 mm respectively from the source. Based on Eqn. 2.20 the relative amplitude of the acoustic response scales proportional to $(1/\mu)(c_p/c_s)^2$ for a given impulse on target, which comparing aluminum and steel would predict a 3.89 times larger response in aluminum compared to steel. Based on this simple scaling the 2.1 nm peak-to-peak amplitudes at 13 mm from the source for steel would correspond to 8.2 nm in aluminum for an 80 mJ Nd:YAG laser pulse. This would be considerably less than the 23 nm response observed in the present experiment with a 40 mJ KrF laser pulse. The second study reported a peak-to-peak SAW amplitude of 6 nm for a probe-source separation of 19 mm from the source on a 4.7 mm thick aluminum plate. From Eqn. 5.3, the mechanical coupling scales as $\lambda^{-0.301}$ and $\tau_{ns}^{0.1505}$ for similar energy laser pulses. As a consequence of the longer pulse width of 30 ns and longer wavelength of 1.064 µm, the mechanical coupling for similar intensities would therefore be 1.3 times lower than ours at 10 ns and 248 nm. Therefore the reported SAW amplitude of 6 nm would be equivalent to a value of 7.9 nm peak-to-peak for our laser conditions if the focal spots were the same. From the results for $d_{probe} = 20$ mm, a peak-to-peak amplitude of 11.3 nm at 25 mJ from Fig 4.4 (b) was measured. Scaling this value to a distance $d_{probe} = 19$ mm based on the $d_{probe}^{-1/2}$ scaling, a peak-to-

peak displacement of 11.7 nm would be expected. This is somewhat larger than the previously reported result. However the focal spot conditions may be different in the two cases and the longer wavelength 1.064 µm laser would be subject to plasma shielding from the breakdown of air on front of the surface. The shorter excitation wavelength of 248 nm for the KrF laser is better absorbed in the aluminum target and is very little perturbed by the air breakdown because of the low plasma density in air compared to the critical density plasma density at 248 nm. Thus it might be expected that the use of an ultraviolet laser may lead to better coupling and lead to the excitation of larger amplitude SAWs due to reduced plasma shielding. A recent study [3] has demonstrated the generation of very large amplitude SAW generation in Al 6061 using Nd:YAG laser pulses, focused onto a carbon powder was deposited as a thin layer (~100 µm) onto the surface of the sample. By integrating Fig. 3(b) in reference [3], which is a plot of the measured normal surface velocity of the SAW for a source-to-probe separation of 26.7 mm, one would calculate a peak-to-peak SAW amplitude of 1.03 µm using a laser pulse energy of up to 100 mJ with a pulse duration of 26 ns. The beam was focused down to a line of dimension 10 mm by ~10 µm. The thin layer of the carbon suspension was employed to optimize the absorption of the infrared light. It is believed that the very large acoustic amplitude arises from the fact that the laser light is focused into a very narrow strip. Since the line is approximately 10 µm wide, the acoustic impulse is concentrated into a much smaller region. One would expect that the peak-to-peak amplitude of the SAW must be larger for the same impulse delivered to the target. At the same time, the acoustic pulse is much shorter in duration with a crest-to-valley temporal

separation of 50 ns (from integrating Fig. 2 in [3]) and 92 ns (from integrating Fig. 3(b)

in [3]) which indicates that there are very high frequency components in the SAW.

6 – Conclusion

An all-optical means for generating and detecting surface acoustic waves has been examined. Using ultraviolet laser pulses, large amplitude SAWs have been produced by ablative generation in aluminum 6061 samples. By using a calibrated commercial interferometer, the SAW parameters under varying laser and detection conditions have been studied in order to quantify the generation of SAWs from ultraviolet laser pulses.

In examining the SAW waveform, several phenomena were observed. The polarity of the ablatively generated SAW was found to be such that the leading edge of the wave should have a peak outward displacement from the sample surface, followed by a peak inward displacement into the sample surface. The average crest-to-valley ratio was found to vary slightly as a function of the source-to-probe distance, which is believed to be due to the small frequency dependent scattering and absorption factor for the SAW as it propagates, which is also indicated by the variation in the peak SAW frequency as a function of source-to-probe separation. There was a step displacement after the main SAW pulse on the order of a nanometer. This step was attributed to the pressure caused by the residual blast wave in air produced by the plasma. The blast wave in air itself was measured several microseconds after the appearance of the SAW as a perturbation in the index of refraction in air.

The amplitude of the SAW was found to vary as a function of pulsed laser energy, which obeyed an amplitude scaling law of $E^{(0.71 \text{ to } 0.85)}$. The SAW amplitude was also found to depend on the intensity of the laser spot, by varying the position of the focusing lens. This result demonstrated a maximum acoustic coupling at an intensity of 4.1×10^9 Wcm^{-2} at a position 2 mm out of focus for our experimental conditions yielding a

response 1.5 times higher than at best focus. This increase compared reasonably to the expected 1.33 times increase in acoustic coupling as predicted by the analytical plasma model and a 1.42 times increase in acoustic coupling as predicted by an empirical model. The amplitude dependence on the source-to-probe separation was examined for both a spot and line geometry. For a spot source, the amplitude was found to deviate somewhat from the expected $d^{1/2}$ dependence, with an exponential attenuation coefficient of $a =$ 0.009 mm^{-1} which may be attributed to acoustic scattering or absorption in the material. This may be due to surface roughness or microstructure and residual stresses in the material. This attenuation coefficient is an order of magnitude larger than the previously reported attenuation measurements made on duraluminum. The SAW velocity was measured to a high degree of accuracy and precision on the order of 0.15%.

Careful examination of the laser spot geometry by using a CCD camera, and by examining the laser produced craters on the surface of the aluminum samples have revealed important information about the intensity of the beam, and has proven useful in modeling the SAW waveform. The SAW waveform was modeled by using the Green's function for a Heaviside step function. By using a cosine-squared force profile in time that correspond to the acoustic wave propagation time across the interaction region, and by calculating the impulses delivered to the aluminum targets based on previous work, the calculated SAW wave forms could be closely matched to the experimental SAW waveforms. Cosine-squared base-to-base pulse durations of $T = 225$ ns and $T = 135$ ns with peak values of forces of 6.2 N and 1.6 N, for SAWs generated by 40 mJ KrF laser pulses and 5 mJ 4th harmonic Nd:YAG laser pulses respectively were found to give good overall agreement with the experimental SAW waveforms. This was done by taking an

average match of the model's crest to valley time duration and the full width at half minimum for the valley of the SAWs to the experimental waveforms.

The impulse required to match the experimental measurements for the KrF laser pulses and 4th harmonic Nd:YAG laser pulses was 90% and 91% respectively of the impulse predicted by a parametric scaling law derived from a compilation of experimental data for ablation of aluminum. The impulses were also 63% and 59% of the values predicted by a simple self-similar plasma ablation model for the KrF laser pulses and 4th harmonic Nd:YAG pulses respectively. The amplitudes measured here are considerably larger than those previously reported on steel, and somewhat larger than those previously reported for aluminum using infrared laser single spot excitation pulses. These amplitudes greatly exceed those generated by thermoelastic excitation of materials and demonstrate the effectiveness of using ultraviolet lasers in the ablative excitation regime for the generation of large amplitude surface acoustic waves.

References

[1] C. B. Scruby and L. E. Drain, *Laser Ultrasonics: Techniques and Applications*. Bristol, England: Adam Hilger, 1990.

[2] J. -D. Aussel and J. -P. Monchalin, "Precision laser-ultrasonic velocity measurement and elastic constant determination," *Ultrasonics*, vol. 27, pp. 165-177, 1989.

[3] A A. Kolomenskii and H. A. Schuessler, "Characterization of isotropic solids with nonlinear surface acoustic wave pulses," *Phys. Rev. B.*, vol. 63, pp. 5413-5418, 2001.

[4] S. Fassbender, B. Hoffmann, and W. Arnold, "Efficient generation of acoustic pressure waves by short laser pulses," *Mater. Sci. Eng.*, vol. A122, pp. 37-41, 1989

[5] D. A. Hutchins, R. J. Dewhurst, and S. B. Palmer, "Directivity patterns of laser-generated ultrasound in aluminum," *J. Acoust. Soc. Am.*, vol. 70, pp. 1362-1369, 1981.

[6] R. J. Dewhurst, C. Edwards, A. D. W. McKie, and S. B. Palmer, "Estimation of the thickness of thin metal sheet using laser generated ultrasound," *Appl. Phys. Lett.*, vol. 51, pp. 1066-1068, 1987.

[7] L. Wu, J. -C. Cheng, and S. -Y. Zhang, "Mechanisms of laser-generated ultrasound in plates," *J. Phys. D.: Appl. Phys.*, vol. 28, pp. 957-964, 1995.

[8] V. E. Chabanov, "Study of the characteristics of acoustic signals excited by a moving laser beam," *Russian Journal of Nondestructive Testing*, vol. 34, pp. 636-644, 1998.

[9] S. J. Davies, C. Edwards, G. S. Taylor, and S. B. Palmer, "Laser-generated ultrasound: its properties, mechanisms and multifarious applications," *J. Phys. D.: Appl. Phys.*, vol. 26, pp. 329-348, 1993.

[10] T. Sanderson, C. Ume, and J. Jarzynski, "Laser generated ultrasound: a thermoelastic analysis of the source," *Ultrasonics*, vol. 35, pp. 115-124, 1997.

[11] L. R. F. Rose, "Point-source representation for laser-generated ultrasound," *J. Acoust. Soc. Am.*, vol. 75, pp. 723-732, 1984.

[12] C. B. Scruby, R. J. Dewhurst, D. A. Hutchins, S. B. Palmer, "Laser generation of ultrasound in metals," in *Research Techniques in Nondestructive Testing*, vol. 5, p. 281, edited by R. S. Sharpe, New York: Academic, 1982.

[13] M. G. Silk, *Ultrasonic Transducers for Nondestructive Testing*. Bristol, England: Adam Hilger, 1984.

[14] E. Bourkoff and C. H. Palmer, "Low-energy optical generation and detection of acoustic pulses in metals and nonmetals," *Appl. Phys. Lett.*, vol. 46, pp. 143-145, 1985.

[15] C. M. Scala and P. A. Doyle, "Time- and frequency-domain characteristics of laser-generated ultrasonic surface waves," *J. Acoust. Soc. Am.*, vol. 85, pp. 1569-1576, 1989.

[16] C. B. Scruby and B. C. Moss, "The launching of Rayleigh waves from surface point sources," from *Rayleigh-Wave Theory and Application*, edited by E. A. Ash and E. G. S. Paige. New York: Springer, 1985.

[17] A. M. Aindow, J. A. Cooper, R. J. Dewhurst, and S. B. Palmer, "A spherical capacitance transducer for ultrasonic displacement measurements in NDE," *J. Phys. E: Sci. Instrum.*, vol. 20, pp. 204-209, 1987.

[18] P. Krehl, F. Schwirzke, and A. W. Cooper, "Correlation of stress-wave profiles and the dynamics of the plasma produced by laser irradiation of plane solid targets," *J. Appl. Phys.*, vol. 46, pp. 4400-4406, 1975.

[19] P. Mora, "Theoretical model of absorption of laser light by a plasma," *Phys. Fluids*, vol. 25, pp. 1051-1056, 1982.

[20] C. L. Pekeris, "The seismic surface pulse," *Geophysics*, vol. 41, pp. 469-480, 1955.

[21] H. M. Mooney, "Some numerical solutions for Lamb's problem," *Bulletin of the Seismological Society of America*, vol. 64, pp. 473-491, 1974.

[22] H. M. Mooney, "The seismic wave system from a surface impact," *Geophysics*, vol. 41, pp. 243-265, 1976.

[23] G. W. Rieger, M. Taschuk, Y. Y. Tsui, and R. Fedosejevs, "Laser-induced breakdown spectroscopy for microanalysis using submillijoule UV laser pulses," *Appl. Spectrosc.* Vol. 56, pp. 689-698, 2002.

[24] Precision Optical Displacement Sensor (PODS), MPB Technologies, Inc., Montreal, Quebec, Canada.

[25] EX540 Excimer Laser, Lumonics, Inc., Kanata, Ontario, Canada.

[26] Ultra CFR Nd:YAG Laser, Big Sky Laser Technologies, Bose, Montana.

[27] Dylux Proofing Paper, Du Pont Corporation. Itasca, Illinois.

[28] P. Hariharan, *Basics of Interferometry*. Toronto, Canada: Academic Press, 1992.

[29] J. -P. Monchalin, J. -D. Aussel, R. Héon, C. K. Jen, A. Boudreault, and R. Bernier, "Measurements of in-plane and out-of-plane ultrasonic displacements by optical heterodyne interferometry," *J. Nondestr. Eval.* vol. 8, pp. 121-133, 1989.

[30] PODS Precision Optical Displacement Sensor User Manual, MPB Technologies, Inc., Montreal, 1999.

[31] R. E. Simpson, *Introductory Electronics for Scientists and Engineers, 2nd Edition.* Englewood Cliffs, New Jersey: Prentice Hall, 1987.

[32] Miniature DC to HV DC Converter Model G03, EMCO High Voltage Corporation, Sutter Creek, California.

[33] EDC-1000HR CCD Camera, Electrim Corporation, Princeton, New Jersey.

[34] L. M. Cabalín and J. J. Laserna, "Experimental determination of laser induced breakdown thresholds of metals under nanosecond Q-switched laser operation," *Spectrochimica Acta Part B*, vol. 53, pp. 723-730, 1998.

[35] A. A. Kolomenskii and P. Hess, "UV laser excitation of broadband surface acoustic wave pulses in silicon near the ablation threshold," *1994 Ultrasonics Symposium*, pp. 651-654, 1994.

[36] C. R. Phipps Jr., T. P. Turner, R. F. Harrison, G. W. York, W. Z. Osborne, G. K. Anderson, X. F. Corlis, L. C. Haynes, H. S. Steele, K. C. Spicochi, and T. R. King, "Impulse coupling to targets in vacuum by KrF, HF, and CO_2 single-pulse lasers," *J. Appl. Phys.*, vol. 64, pp. 1083-1095, 1988.

[37] P. D. Gupta, Y. Y. Tsui, R. Popil, R. Fedosejevs, and A. A. Offenberger, "Ablation parameters in KrF laser/plasma interaction: An experimental study," *Phys. Fluids*, vol. 30, pp. 179-185, 1987.

[38] T. Efthimiopoulos, E. Kritsotakis, H. Kiagias, C. Savvakis, and Y. Bertachas, "Laser ablation rate of materials using the generated acoustic waves," *J. Phys. D: Appl. Phys.*, vol. 31, pp. 2648-2652, 1998.

[39] X. Xu and K. H. Song, "Diagnostics of laser plasma interaction," Proc. SPIE, vol. 3935, pp. 24-31, 2000.

[40] P. A. Doyle and C. M. Scala, "Near-field ultrasonic Rayleigh waves from a laser line source," *Ultrasonics*, vol. 34, pp. 1-8, 1996.

[41] A. P. Mayer and M. Lehner, "Effect of random surface and interface roughness on the propagation of surface acoustic waves," *Waves in Random Media*, vol. 4, pp. 321-335, 1994.

[42] M. de Billy, G. Quentin, and E. Baron, "Attenuation measurements of an ultrasonic Rayleigh wave propagating along rough surfaces," *J. Appl. Phys.*, vol. 61, pp. 2140-2145, 1987.

[43] T. Lyman *editor, Metals Handbook 8th Edition volume 1: Properties and Selection of Metals*, Metals Park, Ohio: American Society for Metals, 1961.

[44] L. F. Mondolfo, *Aluminum Alloys: Structure and Properties*, Toronto, Ontario: The Butterworth Group, 1976.

[45] D. R. Lide *editor-in-chief, CRC Handbook of Chemistry and Physics 83rd Edition*, New York, NY: CRC Press, 2002.

[46] Sir G. Taylor, "The formation of a blast wave by a very intense explosion. I. Theoretical discussion," *Proceedings of the Royal Society of London. Series A, Mathematical and Physical Sciences*, vol. 201, pp. 159-174, 1950.

[47] H. L. Brode, "Numerical solutions of spherical blast waves," *J. Appl. Phys.*, vol. 26, pp. 766-776, 1955.

[48] H. H. Goldstine and J. von Neumann, "Blast wave calculation," *Commun. Pure Appl. Math.*, vol. 8, pp. 327-354, 1955.

[49] M. V. Ötügen and B. Ganguly, "Laser heterodyne method for high-resolution gas-density measurements," *Appl. Opt.*, vol. 40, pp. 3502-3505, 2001.

[50] J. P. Gospodyn, A. Sardarli, A. M. Brodnikovski, and R. Fedosejevs, "Ablative generation of surface acoustic waves in aluminum using ultraviolet laser pulses," *J. Appl. Phys.*, vol. 92, pp. 564-571, 2002.

[51] Sesame: The Los Alamos National Laboratory Equation of State Database, Los Alamos National Laboratory Report.

[52] A. Neubrand and P. Hess, "Laser generation and detection of surface acoustic waves: Elastic properties and surface layers," *J. Appl. Phys.*, vol. 71, pp. 227-238, 1992.